

Spectral appearance of the planetary surface accretion shock: Global spectra and hydrogen-line profiles and luminosities

YUHIKO AOYAMA,^{1,2,3} GABRIEL-DOMINIQUE MARLEAU,^{4,5,6} CHRISTOPH MORDASINI,⁵ AND MASASHIRO IKOMA¹

¹*Department of Earth and Planetary Science, University of Tokyo, 7-3-1 Hongo, Bunkyo-ku, Tokyo 113-0033, Japan*

²*Institute for Advanced Study, Tsinghua University, Beijing 100084, People's Republic of China*

³*Department of Astronomy, Tsinghua University, Beijing 100084, People's Republic of China*

⁴*Institut für Astronomie und Astrophysik, Universität Tübingen, Auf der Morgenstelle 10, 72076 Tübingen, Germany*

⁵*Physikalisches Institut, Universität Bern, Gesellschaftsstr. 6, 3012 Bern, Switzerland*

⁶*Max-Planck-Institut für Astronomie, Königstuhl 17, 69117 Heidelberg, Germany*

(Received —; Revised —; Accepted —)

Submitted to ApJ

ABSTRACT

Hydrogen-line emission from an accretion shock has recently been observed at planetary-mass objects. Previous work predicted the shock spectrum and luminosity for a shock on the circumplanetary disc. We extend this to the planet-surface shock. We calculate the global spectral energy distribution (SED) of accreting planets by combining our model emission spectra with photospheric SEDs, and predict the line-integrated flux for several hydrogen lines, especially $H\alpha$, but also $H\beta$, $P\alpha$, $P\beta$, $P\gamma$, $Br\alpha$, and $Br\gamma$. We apply our non-equilibrium emission model to the surface accretion shock for a wide range of accretion rates \dot{M} and masses M_p . Fits to formation calculations provide radii and effective temperatures. Extinction by the surrounding material is neglected, which is arguably often relevant. We find that the line luminosity increases monotonically with \dot{M} and M_p , depending mostly on \dot{M} and weakly on M_p for the relevant range of parameters. The Lyman, Balmer, and Paschen continua can exceed the photosphere. The $H\beta$ line is fainter by 0–1 dex than $H\alpha$, whereas other lines are weaker (by ~ 1 –3 dex). Shocks on the planet or the CPD surface are distinguishable at very high spectral resolution, but the planet surface shock likely dominates if both are present. Applied to recent non-detections of $H\alpha$, our models imply looser constraints on the \dot{M} of putative planets than from stellar extrapolations. These hydrogen-line luminosity predictions are useful for interpreting (non-)detections of accreting planets.

Keywords: Exoplanet formation (492); Accretion (14); Shocks (2086); Hydrogen lines [H I line emission] (690); H alpha photometry (691); Direct imaging (387); High resolution spectroscopy (2096)

1. INTRODUCTION

Recent instrumental improvement have enabled the observation of forming planets (e.g. Kraus & Ireland 2012; Quanz et al. 2013; Currie et al. 2015; Wagner et al. 2018). Because it is expected to yield information on how planets grow, the detection of $H\alpha$ is particularly important (Sallum et al. 2015; Wagner et al. 2018; Haffert et al. 2019; Cugno et al. 2019; Zurlo et al. 2020; Xie et al. 2020).

In the context of forming low-mass protostars (Classical T Tauri stars: CTTS), $H\alpha$ is known as an indicator of accretion and used to estimate mass accretion rate (e.g. Gullbring et al. 1998). The $H\alpha$ from CTTS is brighter than the photospheric continuum by a few mag and has large width ($\gtrsim 200$ km s⁻¹). The magnetospheric accretion model (Uchida & Shibata 1984; Königl 1991) can explain these char-

acteristic features when the accretion funnel is hot enough to emit $H\alpha$ (e.g. Hartmann et al. 1994; Muzerolle et al. 2001). Furthermore, the line-integrated luminosity ($L_{H\alpha}$) or the spectral width ($\Delta\lambda_{H\alpha}$) of the $H\alpha$ line shows a correlation to the mass-accretion rate (or accretion luminosity, L_{acc}) estimated with modeling of continuum emission (e.g. Valenti et al. 1993; Calvet & Gullbring 1998). Therefore, $H\alpha$ is used to estimate the accretion rate for protostars that are too far for their continuum emission to be observable (e.g. Gullbring et al. 1998; Herczeg & Hillenbrand 2008; Fang et al. 2009; Rigliaco et al. 2012; Alcalá et al. 2014, 2017; Natta et al. 2004). Similar statements hold for further hydrogen lines from the Balmer, Paschen, Brackett, or other series.

As with the stellar cases, the $H\alpha$ excess was reported from protoplanets, and the observed luminosity was used to estimate the accretion rate by applying the results of the CTTS

observations (Sallum et al. 2015; Wagner et al. 2018; Haffert et al. 2019). However, there is no guarantee that relationships between L_{acc} and $L_{\text{H}\alpha}$ or $\Delta\lambda_{\text{H}\alpha}$ given in CTTS are valid for protoplanets. Thanathibodee et al. (2019) applied the stellar H α emission model of Muzerolle et al. (2001) to a planetary-mass object (PDS 70 b) and argued the $L_{\text{H}\alpha}$ - L_{acc} relationship shows a different trend from that of protostars (Ingleby et al. 2013; Rigliaco et al. 2012; see also Szulagyi & Ercolano 2020 and the discussion of their work in Aoyama et al. submitted).

Planetary gas accretion is qualitatively different from the stellar one in some points. An important characteristic feature is that protoplanets and their surrounding gaseous disk (circum-planetary disk, CPD) are embedded in the stellar surrounding disk (protoplanetary disk, PPD). On the way of gas accreting towards the protoplanet, the gas preferentially enters the planetary gravitational sphere in high altitudes above the disk midplane (e.g. Tanigawa et al. 2012). When the gas falling from the PPD to CPD vertically hits the CPD surface, it yields a strong shock, which can be hot enough to emit H α (Szulagyi & Mordasini 2017). Aoyama et al. (2018) constructed a model of shock-heated gas with cooling, chemical reactions, and radiative transfer, estimated hydrogen line luminosity depending on the gas velocity and density, and estimated the $L_{\text{H}\alpha}$ depending on the shock properties.

On the other hand, the magnetospheric accretion may occur even in the planetary accretion, bringing about a strong shock also on the planetary surface. If protoplanets have dipole magnetic fields strong enough to control the gas dynamics, vertical accretion can occur directly onto the planetary surface (Batygin 2018). While the accretion shock on the CTTS surface is too strong and makes gas too hot to emit H α (see e.g., Hartmann et al. 2016), the weak gravity of protoplanets leads to moderate free-fall velocity ($\sim 100 \text{ km s}^{-1}$) and to emitting a significant amount of H α . In contrast, in the CPD surface shock model, only a small fraction ($\lesssim 1\%$) can contribute to the H α emission, because most gas hits the CPD far from the planet (Aoyama et al. 2018). Also, in the magnetospheric accretion-funnel model, the heating mechanism is still an open question (Muzerolle et al. 2001). Therefore, the gas in the accretion funnel could be too cool to emit H α , perhaps especially for protoplanets not much more massive than Jupiter.

This motivates us, in this study, to model the hydrogen line emission coming from the planetary surface shock, considering a wide range of parameters. We focus on H α first and then explore other hydrogen line emission. We combine these results with models of the photospheric emission and discuss when the shock lines are visible above the photosphere emission. Note that part of the planetary surface shock model presented here was used already in Aoyama & Ikoma (2019) for the case of PDS 70 b and c. A more extensive investigation is done in this study.

The paper is organized as follows: In Section 2 we discuss the properties of the planetary-surface shock and of the planets and review our numerical shock model, which was introduced in Aoyama et al. (2018). In Section 3 we present emission spectra of accreting gas giants for a large grid of models, before applying this in Section 4 to a few objects, especially to their detection at H α . In Section 5 we explore other observational aspects, including line strengths for lines other than H α and the possibility of breaking some degeneracies. Finally, we present a critical discussion in Section 6 before summarizing in Section 7. The appendices present further material: a discussion of our approach compared to Storey & Hummer (1995) (Appendix A), the inverse relationship between the shock-microphysical and planet-formation parameters (Appendix B), a map of the H α luminosity for the cold-start radius fits (Appendix C), and the calculation of the H α luminosity in Wagner et al. (2018) (Appendix D).

2. DESCRIPTION OF THE COMBINED MODEL

We model the spectral energy distribution (SED) of an accreting gas giant with a surface accretion shock. The radiation from the accreting gas giant is mainly composed of two components, namely the photospheric radiation and the shock excess. We assume that the two components can be computed separately, i.e., that the layers heated by the shock do not affect significantly the rest of the emission. For convenience, the planet radius and effective temperature are derived from a specific detailed planet formation and structure model, as detailed in Section 2.1. We consider here the case that the planetary emission (photosphere and shock) is not extinguished, and detail in Section 2.3 when this is relevant.

For the photospheric radiation model, we use the CIFIST2011_2015 BT-Settl models, which calculated spherical radiative transfer in atmospheres with solar metallicity¹ (Allard et al. 2012; Baraffe et al. 2015). The shock excess is calculated from the 1D radiation-hydrodynamic model developed by Aoyama et al. (2018) and Aoyama & Ikoma (2019), which is outlined in Section 2.2. We contrast our model of the shock emission to Storey & Hummer (1995) in Appendix A.

In this study, we focus on the shock-heated gas on the planetary surface. We treat only the emission from the photosphere and shock-heated gas but not from the CPD, whose temperature is lower than those of the photosphere and the shock. Continuum emission from a (simplified) CPD model has been calculated in Zhu (2015), Eisner (2015), and Szulagyi et al. (2019), and the line emission from the shock on the CPD has been calculated in Aoyama et al. (2018).

2.1. Fitting of planetary properties

¹ From https://phoenix.ens-lyon.fr/Grids/BT-Settl/CIFIST2011_2015/.

The input parameters for our combined spectra of the accretion shock and the photosphere are mass accretion rate \dot{M} , planet mass M_p , planet radius R_p , filling factor f_{fill} of the shock on the planet surface, and photospheric effective temperature T_{eff} . However, taking them as independent would result in an impractically large parameter space and may lead to unlikely combinations (e.g., small radius and mass but large luminosity). Therefore, only the accretion rate, the planet mass, and the filling factor will be considered as free parameters. A discussion of how the accretion geometry sets f_{fill} is given in [Marleau et al. \(subm., see their Figure 1\)](#).

2.1.1. Radius fit

In principle, the main parameter space for our calculations is $(\dot{M}, M_p, R_p, f_{\text{fill}})$ along with the choice of “cold-start” or “hot-start” accretion (high or low radiation efficiency of the accretion energy; [Marleau et al. 2017, 2019](#)). Here, we take for the sake of definiteness the $R_p(\dot{M}, M_p)$ relations in the cold- and hot-start populations of the Bern model ([Alibert et al. 2005; Mordasini et al. 2012b,a, 2015, 2017](#)), using data from all time snapshots². We use the populations CD752 (hot) and CD753 (cold), described and analysed in [Mordasini et al. \(2012b,a, 2017\)](#) (Generation Ib). Recently, the first results from the Generation III population syntheses of the Bern model were released ([Emsenhuber et al. 2020a,b; Schlecker et al. 2020](#)), which all assume warm accretion. We verified that the distribution of points in (\dot{M}, M_p, R_p) space is very similar between the 1- and the 100-embryo-per-disk simulations NG73 and NG76, respectively, on the one hand, and CD752 on the other. Two small differences are that the accretion rates reached are not quite as high as in Generation Ib (note however that there are fewer synthetic planets in the region of interest), and that in NG76 the radii can be higher at a given \dot{M} and M_p , likely due to interactions between the embryos. Since the radii are overall similar, we will keep using the Generation Ib populations in order to cover also high accretion rates, as could be relevant for instance to accretion outbursts (e.g., [Lubow & Martin 2012; Brittain et al. 2020; Martin et al. 2021](#)).

These planet structure models were calculated assuming that the planet is at all times convective. Recent work suggests that forming planets may be in fact in part radiative ([Berardo et al. 2017; Berardo & Cumming 2017; Cumming et al. 2018](#)) and thus have a different radius. Nevertheless, the relations $R_p(\dot{M}, M_p)$ from the population syntheses provide a reasonable bracket and reduce the dimensionality of the large parameter space $(\dot{M}, M_p, R_p, \eta, f_{\text{fill}}, \dots)$. However, it is clear that this is not meant as a final answer and one could

repeat this study with for example the $R_p(\dot{M}, M_p)$ relations of [Ginzburg & Chiang \(2019\)](#), who find (much) larger radii at a given mass.

After some experimentation, we arrived at the following relatively simple form for the fitting function³:

$$R_1(\dot{M}, M_p) = a_0 + b_0 \lg \dot{M}_2 + c_0 e^{d_0 \lg \dot{M}_2} + (a_1 + b_1 \lg \dot{M}_2 + c_1 e^{d_1 \lg \dot{M}_2})(M_1 - 1) + (a_2 + b_2 \lg \dot{M}_2 + c_2 e^{d_2 \lg \dot{M}_2})(M_1 - 1)^2, \quad (1)$$

where $R_1 \equiv R_p/R_J$, $M_1 \equiv M_p/M_J$, and $\lg \dot{M}_2 \equiv \log_{10}(\dot{M}/10^{-2} M_E \text{ yr}^{-1})$. The fits were performed through `gnuplot`'s built-in `fit` routine. Only planets with $\dot{M} > 10^{-5} M_E \text{ yr}^{-1}$, $1 M_J < M_p < 20 M_J$, and $R_p < 4 R_J$ were used to obtain the fits. We used for each planet a statistical weight inversely proportional to its radius to have a more accurate fit at lower radii, for which v_0 is higher and thus the accretion signatures a priori stronger. The coefficients for the cold-nominal population are

$$\begin{aligned} a_0 &= 1.53; & b_0 &= 0.111; \\ c_0 &= 1.06; & d_0 &= 0.906; \\ a_1 &= -0.195; & b_1 &= -0.0307; \\ c_1 &= 0.0977; & d_1 &= 0.000695; \\ a_2 &= -0.250; & b_2 &= 0.000276; \\ c_2 &= 0.254; & d_2 &= 0.000214 \end{aligned}$$

and for the warm population the coefficients are

$$\begin{aligned} a_0 &= 0.411; & b_0 &= -0.244; \\ c_0 &= 3.45; & d_0 &= 0.762; \\ a_1 &= -0.489; & b_1 &= -0.0961; \\ c_1 &= 0.652; & d_1 &= 0.353; \\ a_2 &= -0.228; & b_2 &= -0.00106; \\ c_2 &= 0.226; & d_2 &= 0.000220. \end{aligned}$$

We verified that excluding from the fitting procedure the planets for which the accretion radius $R_{\text{acc}} < 10R_p$ (this concerns only a small fraction of the planets) changed neither the relationships nor the quality of the fit significantly. The accretion radius R_{acc} is a spherically-averaged estimate of the typical distance from which the gas is effectively falling onto the planet. It is defined through

$$\frac{1}{R_{\text{acc}}} = \frac{1}{R_{\text{Bondi}}} + \frac{1}{k_{\text{Liss}} R_{\text{Hill}}}, \quad (2)$$

where R_{Bondi} and R_{Hill} are the Bondi and Hill radii and $k_{\text{Liss}} = 1/4$ (and not $k_{\text{Liss}} = 1/3$ as in [Mordasini et al. 2012b](#)).

The resulting relations $R_p(\dot{M}, M_p)$ for the cold-nominal and the warm populations are shown in [Figure 1](#). At high

² The data can be visualized at, and downloaded from, the “Evolution” section of the Data Analysis Centre for Exoplanets (DACE) platform under <https://dace.unige.ch>.

³ For convenience, it is provided in different languages along with the fit coefficients in the “Suite of Tools to Model Observations of accRetIng planeTZ” (St-Moritz) at <https://github.com/gabrielastro/St-Moritz>.

accretion rates, R_p reaches $\approx 5 R_J$ ($\approx 3 R_J$) in the “warm” (“cold-nominal”) population. As a function of mass, the radius monotonically increasing with mass for the “warm population” and has a minimum near $10\text{--}15 M_J$ for the “cold-nominal” population.

The fit is overall excellent, with a match to roughly 10%. For the cold-nominal population, which displays the largest deviations: Only for masses $M_p \gtrsim 15 M_J$ near $\dot{M} = 10^{-4}\text{--}10^{-3} M_E \text{ yr}^{-1}$ is the function too small, by at most only $\approx 30\%$, and at $\dot{M} \gtrsim 3 \times 10^{-2} M_E \text{ yr}^{-1}$ for M_p between 1 and $10 M_J$ larger or smaller by at most $\approx 30\%$. This reflects in part the intrinsic scatter in the population synthesis results. For the warm population, the fitted function yields radii also at most 30% too small but only towards high masses and low accretion rates. At lower accretion rates and, in the cold-nominal population, for lower masses than shown, the fit re-increases but this matches rather well overall the data (not shown).

2.1.2. Effective temperature

For the photospheric temperature T_{eff} , we adopt a semi-analytical prescription that ensures that, approximately, the total outgoing flux (shock and photosphere) is equal to the sum of the internal and incoming energy flux.

At the shock, a portion of the incoming energy is converted into hydrogen-line and recombination-continua emission. The remaining portion travels downward into the atmosphere, where it is expected to be thermalised because most of the energy is in Ly α , which can easily be thermalised. What matters for the structure of the planet is whether this radiation goes deep into the planet, thereby heating it up, or whether only the top layers are heated up and re-emit the radiation, on a timescale that is short compared to the cooling time of the planet. The former outcome corresponds to the “Hot start (accreting)” case of Mordasini et al. (2012b, their Equation (13)), and the latter to their “Cold start” case. In both cases, the total luminosity just outside the planet⁴ is $L \approx L_{\text{int}} + L_{\text{acc}}$, where L_{int} is the energy coming from the deep interior.

However, the spectrum of the accreting region (covering a fraction f_{fill} of the surface of the planet) differs between the two extreme cases, as noted by Mordasini et al. (2012b). In the “Hot start” extreme case the spectrum is entirely thermalised, as given by an atmospheric model with $T_{\text{eff}}^4 = T_{\text{int}}^4 + T_{\text{acc}}^4$, where the “accretion temperature”

$$T_{\text{acc}} = \left(\frac{L_{\text{acc}}}{4\pi R_p^2 f_{\text{fill}} \sigma} \right)^{1/4}, \quad (3)$$

⁴This does not consider the energy recycling in the accretion flow discussed by Marleau et al. (2017, 2019), and ignores any absorption in the layers closest to the planet; we take $\eta^{\text{kin}} = 1$ for this discussion.

with σ the Stefan–Boltzmann constant. Then there would be no emission-line spectrum as we have been computing in this work. At the other extreme, in the “Cold start” case the spectrum from the accreting region is given by the sum of an atmosphere at $T_{\text{eff}} = T_{\text{int}}$ (i.e., not heated up at all by the shock) and the shock emission. Clearly both are limiting cases. In either case the remaining fraction $(1 - f_{\text{fill}})$ of the planet surface has $T_{\text{eff}} = T_{\text{int}}$, and the global spectral appearance will be a mixture of the spectrum from the accreting and the non-accreting components, with the proportion set by the (rotational-phase-dependent) viewing geometry. We set $f_{\text{fill}} = 1$ in this work for simplicity.

Which scenario is likely more accurate? The single-stream, frequency-averaged simulations of Marleau et al. (2017, 2019) suggest that on the net, only a small fraction of the incoming L_{acc} will go in deeper, but that this small portion is likely (much) higher than the internal luminosity in the extreme cold starts by Marley et al. (2007). However, for the two-stream, frequency-dependent calculations presented here, Aoyama et al. (2018) mentioned that roughly one half of the radiation goes down and one half goes up, which holds in the limit that the emitting region is optically thin. Because the radiation transport is more detailed in the models of Aoyama et al. (2018), we will follow their results. Therefore, we will quantify this fraction more precisely and use it to derive T_{eff} .

Figure 2 shows the fraction f_{down} of the incoming kinetic energy flux that is present in the downward-moving radiation field at the bottom of the computational domain, where T reaches 10^4 K. For this, we have first written

$$f'_{\text{down}} = a_0 + b_0 \text{lg}n_{12} + c_0 \text{lg}n_{12}^2 + \left(a_1 + b_1 \text{lg}n_{12} + c_1 \text{lg}n_{12}^2 \right) \left(v_0 - 100 \text{ km s}^{-1} \right) + a_2 \left(v_0 - 100 \text{ km s}^{-1} \right)^2, \quad (4a)$$

$$f_{\text{down}} = \min \left(\max \left(f'_{\text{down}}, 0 \right), 1 \right), \quad (4b)$$

where $\text{lg}n_{12} \equiv \log_{10} (n_0/10^{12} \text{ cm}^{-3})$. Equation (4b) ensures that f_{down} remains between 0 and 1 and is needed only for a small part of the parameter space, for some models on the grid edge. Using gnuplot’s built-in fit command yielded⁵

$$\begin{aligned} a_0 &= 0.703752; & a_1 &= -0.00527886; \\ b_0 &= -0.0967987; & b_1 &= -0.00146833; \\ c_0 &= -0.0254579; & c_1 &= -0.000321504; \\ a_2 &= -9.91492 \text{ e-}06, \end{aligned}$$

which matches very well the model data (not shown). We had included at first $\text{lg}n_{12}$ terms in the v_0^2 term but their coefficients were consistent with zero. We therefore repeated the fit with

⁵This too is provided in different languages in the “Suite of Tools to Model Observations of accRetIng planeTZ” (St-Moritz) at <https://github.com/gabrielaastro/St-Moritz>.

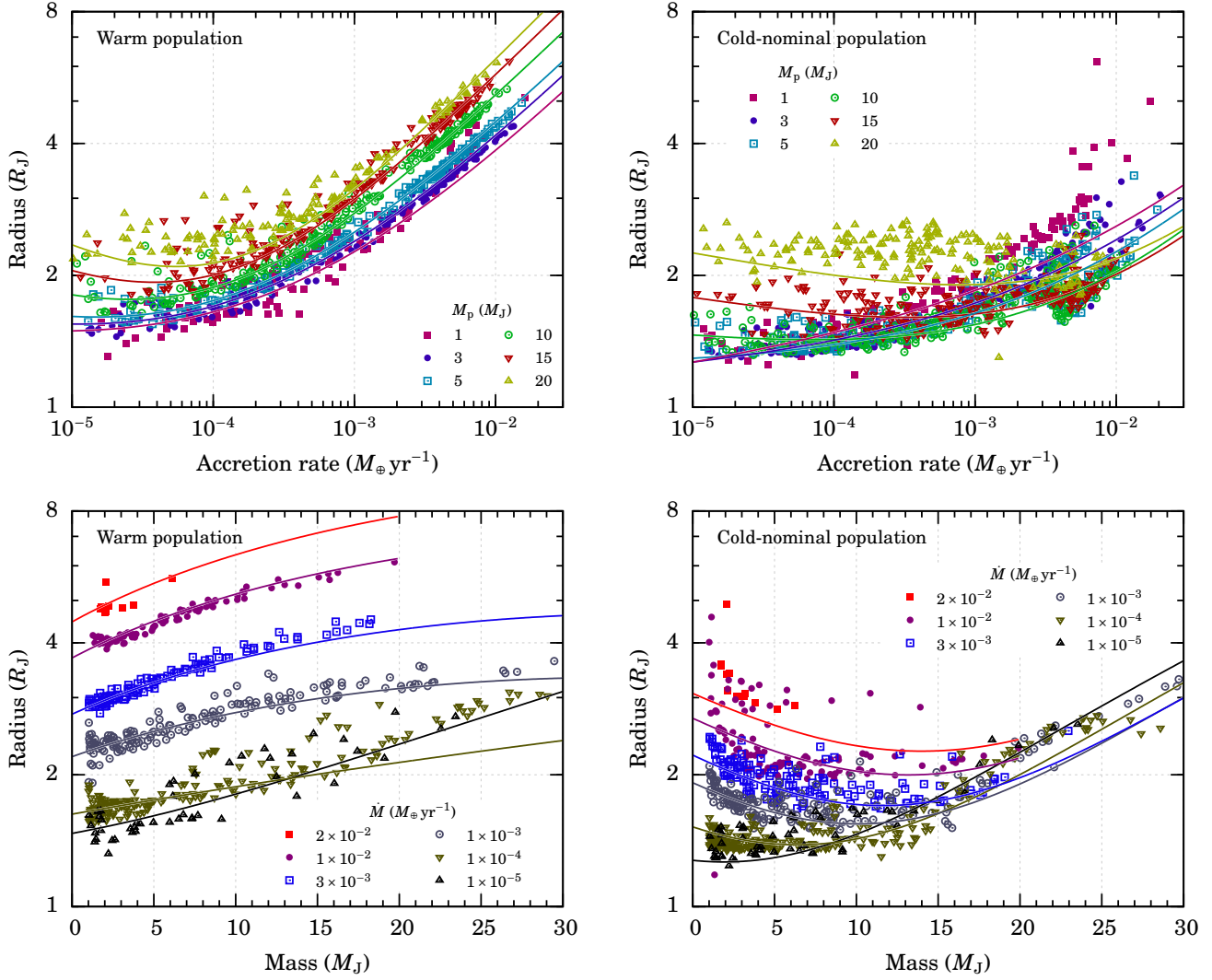


Figure 1. Dependence of the planet radius R_p on accretion rate \dot{M} and planet mass M_p for planets forming by core accretion, for the warm-(cold-)population on the left (right). The population syntheses of Mordasini et al. (2012b) are used but only planets with $R_{\text{acc}} > 20R_p$ are shown. In the top (bottom) row, six masses (accretion rates) are considered (see respective legends). The solid lines display the simple but accurate function of Equation (1) with the fitted coefficient as given in the text. Note the logarithmic vertical scale.

the form of Equation (4a), yielding the reported coefficients. The result of this fit depends only on our grid of models in (n_0, v_0) space and is thus independent of the population. Next, we used Equations (7) and (8), which relate (n_0, v_0) and the macrophysical parameters $(\dot{M}, M_p, R_p, f_{\text{fill}})$ and are presented below, along with the radius fits (Equation (1)) to obtain $f_{\text{down}}(\dot{M}, M_p)$.

We find that the fraction f_{down} does vary at low masses but that it covers mainly $f_{\text{down}} \approx 0.3\text{--}0.8$ between the border of the brown-dwarf region and a few M_J . The fraction depends only relatively weakly on \dot{M} and much more on M_p (through the v_0 dependence), reaching $f_{\text{down}} \approx 1$ at $M_p \approx M_J$. Note that f_{down} is affected to some extent by the non-inclusion of low-temperature ($T \lesssim 10^4$ K) cooling processes at the bot-

tom of the computation domain, for instance from molecules. Currently they are not included, so that in a future model iteration f_{down} could be different, once the inclusion of helium and metals will accelerate the cooling and thus make it computationally feasible to let the simulations cool down to lower temperatures than $T = 10^4$ K. Nevertheless, Figure 2 already provides some guidance.

Having computed f_{down} , we use it to write the photospheric temperature of the accreting region as

$$T_{\text{eff}}^4 = T_{\text{int}}^4 + f_{\text{down}} T_{\text{acc}}^4, \quad (5a)$$

$$\Rightarrow L_{\text{phot}} + L_{\text{shock}} = L_{\text{int}} + L_{\text{acc}}, \quad (5b)$$

where L_{phot} is the luminosity of the photosphere at T_{eff} and L_{shock} is the total shock luminosity. In other words,

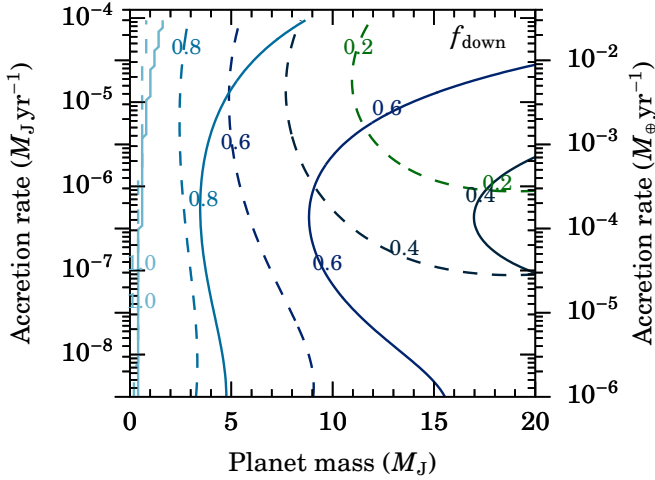


Figure 2. Fraction f_{down} of the incoming kinetic-energy flux that is in the *downward*-travelling radiation field at the bottom of the atmosphere. This includes all hydrogen lines and continua. The solid (dashed) lines use the hot (cold) population radius fits, and for $f_{\text{down}}(n_0, v_0)$ we use the fit from Equation (4).

we assume that the component $F_{\text{down}} = f_{\text{down}}T_{\text{acc}}^4$ from the shock (lines and recombination continua) is thermalised and re-emitted. Equation (5a) ensures that the total upward-travelling radiative flux from our combined models is $F = \sigma T_{\text{eff}}^4 + (1 - f_{\text{down}})\sigma T_{\text{acc}}^4 = \sigma T_{\text{int}}^4 + \sigma T_{\text{acc}}^4$, with the shock flux $F_{\text{shock}} = (1 - f_{\text{down}})\sigma T_{\text{acc}}^4$ contained in the models that are the main subject of this work (see Equation (5b)). In Equation (4), to avoid $T_{\text{eff}} = 0$ K when $f_{\text{down}} = 0$, which occurs at large (\dot{M}, M_p) in the cold-start case, we set somewhat arbitrarily $T_{\text{int}} = 1000$ K. We verified that this barely affects the function $T_{\text{eff}}(\dot{M}, M_p)$. There is a slight effect at $\dot{M} \lesssim 10^{-8} M_J \text{ yr}^{-1}$ but this region of parameter space is of lesser interest.

Figure 3 shows the resulting T_{eff} from Equations (4) and (5a) for both populations for $f_{\text{fill}} = 1$. For the warm-population fit, due to the large radii, T_{eff} ranges only up to ≈ 2500 K, whereas in the cold-population T_{eff} can reach up to 4000 K. Since a logarithmic scale is used for \dot{M} but a linear one for M_p , the dependence of T_{eff} on \dot{M} appears stronger on \dot{M} than on M_p . The low $T_{\text{eff}} \approx 1000\text{--}2000$ K for the cold-population fit at large mass $M_p \approx 20 M_J$ and radius is a consequence of f_{down} going to zero there, with automatically a large sensitivity on the choice of the fit. Thus it should not be taken very seriously, and is not of major concern anyway since this part of parameter is of lesser interest to the present work.

We comment briefly on an implicit assumption we make. When we use standard atmospheric models with Equation (5a), we are assuming that the emission from the heated photosphere can be described by that of an isolated object, i.e., that if the shock changes the pressure–temperature structure of the atmosphere (as it is likely), the resulting spectrum

is not entirely different. This may be a strong simplification, and it would be interesting to explore with dedicated radiative transfer calculations how this modifies the spectral shape.

Spectra for the BT-Settl models we use (CIFIST2011_2015) exist only for $T_{\text{eff}} \geq 1200$ K. Therefore, for the case $T_{\text{eff}} < 1200$ K, we use 1200 K.

2.2. Shock model

2.2.1. Shock parameter space

Locally, a strong shock converts most of the mechanical energy into thermal energy, and the gas temperature increases by orders of magnitude compared to the preshock value. However, since the temperature much exceeds the radiative equilibrium temperature at that point, the shock-heated gas in the postshock region cools rapidly (compared to the postshock flow time) by emitting radiation.

Given the thinness of the radiation-emitting shock layer compared to the planetary radius, we assume the shock on the planetary surface to be one-dimensional as in Aoyama et al. (2018). Then, the shock structure is mainly determined by two input parameters, namely the hydrogen proton number density n_0 and the velocity v_0 before the shock. The preshock temperature of the gas T_0 hardly affects the shock properties, as we discuss below.

As in Aoyama et al. (2018) and e.g. Shapiro & Kang (1987) or Kwan & Fischer (2011), n_0 is defined as the immediate preshock number density of *hydrogen nucleons (protons)* (i.e., contained in H_2 , H I , and H^+ taken together). Thus, contrary to the definition, common in the stellar-structure literature (e.g. Hansen et al. 2004), of n as the number density of all particles, our n_0 is independent of the dissociation and ionization degrees of hydrogen. This definition implies that n_0 is related to the (total) preshock gas mass density ρ_0 by

$$X\rho_0 = n_0 m_{\text{H}}, \quad (6)$$

where X is the hydrogen mass fraction and m_{H} is the mass of a hydrogen atom. We use number ratios given by $\text{H} : \text{He} : \text{C} : \text{O} = 1 : 10^{-1.07} : 10^{-3.48} : 10^{-3.18}$ (Cox 2000). As in Aoyama et al. (2018) we do not consider the other elements, which are negligible. Thus the hydrogen, helium, and metal mass fractions are respectively $X = 0.738$, $Y = 0.251$, and $Z = 1 - X - Y = 0.011$.

In the chemistry module, the abundances of the species are defined by y_i (see also Iida et al. 2001). The quantity y_i is the relative abundance (in number) of species i (of any particle) with respect to the number of hydrogen protons. For example, pure H_2 has $y_{\text{H}_2} = 0.5$. Defining the total $y_t = \sum y_i$, the usual total number density of all particles is given by $n = y_t n_0$; the number density of particles of species i is $n_i = y_i n_0$. With the mean weight per particle given by $\mu_0 = \sum y_i m_i / y_t$ for particle masses $m_i m_{\text{H}}$, we have that $\rho_0 = y_t \mu_0 m_{\text{H}} n_0$, implying $X = 1 / (y_t \mu_0)$.

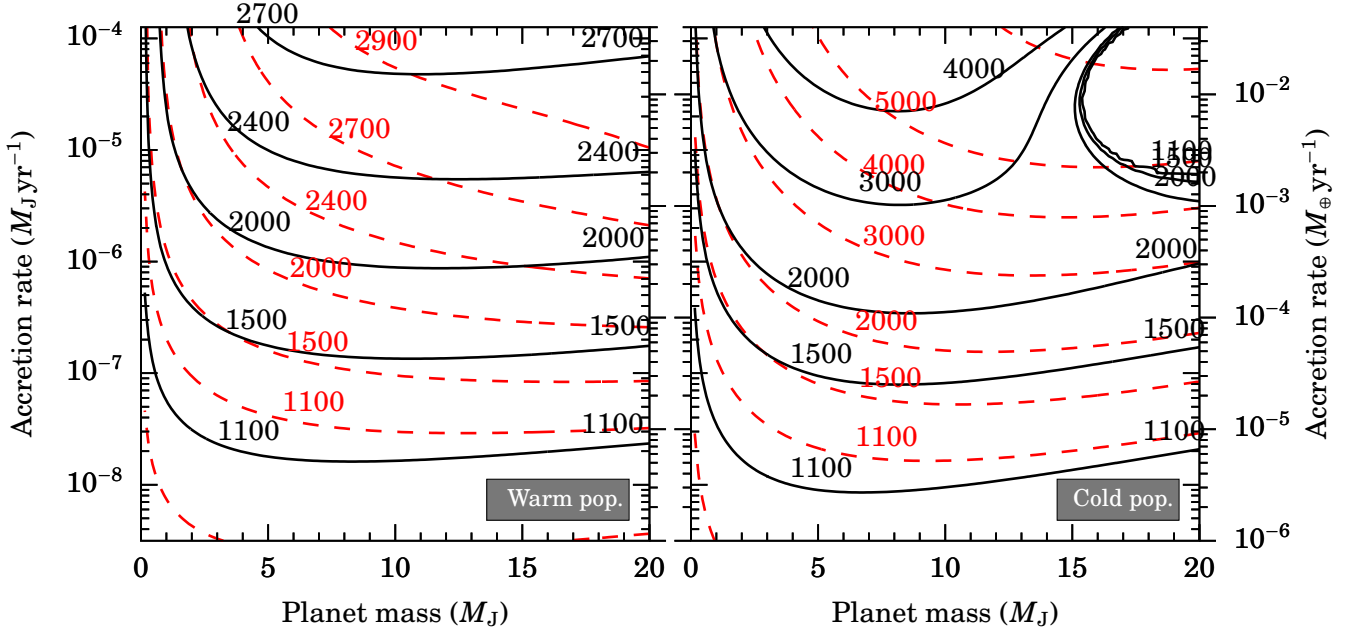


Figure 3. Approximate effective temperature of accreting planets (Equations (4) and (5a), using $T_{\text{int}} = 1000$ K; *black contours*). This is compared to contours of constant T_{acc} (*red dashed contours*). We fix $f_{\text{fill}} = 1$.

The shock input parameters (n_0, v_0) are related to the macrophysical, planet formation parameters ($\dot{M}, M_p, R_p, f_{\text{fill}}$) by

$$v_0 = \sqrt{\frac{2GM_p}{R_p}} \quad (7)$$

$$n_0 = \frac{X\dot{M}}{4\pi R_p^2 f_{\text{fill}} m_H v_0} \quad (8)$$

$$= \frac{X\dot{M}}{\sqrt{32G\pi m_H f_{\text{fill}} \sqrt{M_p R_p^3}}}, \quad (9)$$

where G is the gravitational constant, M_p is the planet mass, R_p is the planet radius, \dot{M} is the accretion rate, and f_{fill} is the filling factor of the shock on the planet surface. Equations (7)–(9) are valid in the limit that the accretion radius $R_{\text{acc}} \gg R_p$, with the gas free-falling from $R_{\text{acc}} \sim R_{\text{Hill}}$ (Equation (2); Bodenheimer et al. 2000). Especially at low masses $M_p \lesssim 1 M_J$, the accreting gas could be falling in at less than the free-fall velocity, depending on the thermodynamics and the angular momentum conservation (Béthune 2019; Schulik et al. 2019, 2020, but note that the finite smoothing length of the latter two works imply that converged results have not quite been reached yet). However, the difference should be small, and for the classical 1D models that we use as an approximation, the limit $R_{\text{acc}} \gg R_p$ usually holds for $M_p \gtrsim 1 M_J$, especially for planets forming at large distances. Similarly, our model is also applicable when the gas falls from the inner edge of the CPD, but, in such a case, the v_0 and the estimated $L_{\text{H}\alpha}$ is smaller by a factor of a few than the results in this pa-

per. Inserting typical values for stars and planets, the typical preshock number density is larger in the planetary than in the stellar case by about a factor of 100 (see Equation (A1)) but one should keep in mind that the parameter space is large.

The assumption here is that all of the accreting gas is available for a shock, whether this turns out to produce $\text{H}\alpha$ or not. In reality, some fraction of the accreting gas could be added to the planet through boundary-layer accretion (BLA; e.g., Kenyon & Hartmann 1987; Kley 1989; Dong et al. 2020), which does not feature supersonic radial velocities. In this scenario, the temperature in the boundary layer would not be high enough for $\text{H}\alpha$ to be emitted. Thus converting an observed $\text{H}\alpha$ luminosity to planetary parameters such as accretion rate and mass needs to assume something about the fraction of the incoming gas that is able to produce $\text{H}\alpha$. Put differently, a measured $\text{H}\alpha$ luminosity yields an estimate of the $\text{H}\alpha$ -emitting accretion rate, while the total accretion rate could be higher. However, it is not clear how likely BLA is in the planetary case; Owen & Menou (2016) argue for BLA but this is based, through the Christensen et al. (2009) scaling, on magnetic field strengths appropriate of old and faint planets ($B \approx 0.03\text{--}0.06$ kG), not forming nor young, high-luminosity (Mordasini et al. 2017) objects, which could have $B \sim 1$ kG (Katarzyński et al. 2016). Thus, assuming that all the accreting gas can undergo a shock seems reasonable, but high-resolution studies are required to help settle the question.

In Figure 4 we plot the preshock velocity as a function of \dot{M} (colour), mass (to be read off from the dashed lines), and

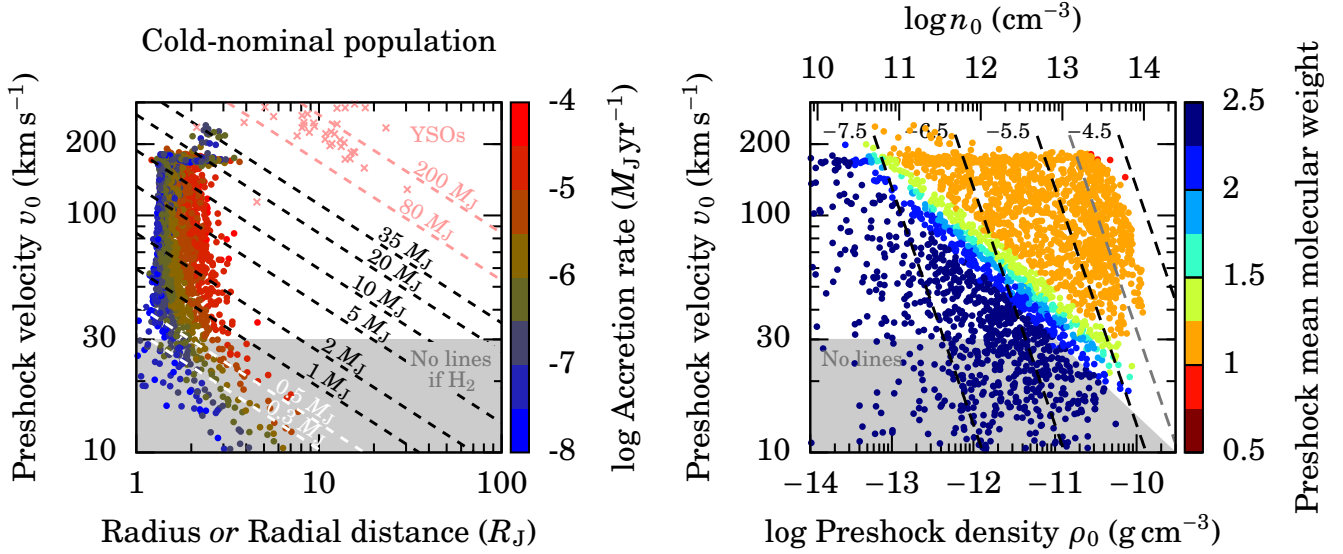


Figure 4. Preshock velocities of forming planets. *Left panel:* Preshock velocity against planet radius or radial distance (for a shock on the CPD). Bern cold-nominal population synthesis planets with $R_{\text{acc}} \geq 10R_p$ are shown, coloured by \dot{M} , and the free-fall velocity (Equation (7)) is drawn for different planet masses (dashed lines). Pink crosses are from the Alcalá et al. (2017) YSO sample. Below $v_0 \approx 30 \text{ km s}^{-1}$, there is no line emission ($H\alpha$, $H\beta$, etc.) if the gas comes in molecular (gray region). *Right panel:* Velocity against mass density or hydrogen proton number density (*lower, upper axes*; Equation (6)). Population synthesis points are shown, colored by the preshock μ_0 (for $\mu_0 \approx 1.3$, only half the points are shown). Dashed lines: constant $\log \dot{M} = -7.5$ to -4.5 ($M_J \text{ yr}^{-1}$) and $R_p = 1.5$ (black) or $3 R_J$ (gray). We fix $f_{\text{fill}} = 1$.

radius planet (x axis) for the cold-nominal Bern population synthesis (Mordasini et al. 2012a, 2017). The hot population objects (not shown) have larger radii but an otherwise similar distribution. All snapshots are included but we restrict $\dot{M} \geq 10^{-8} M_J \text{ yr}^{-1}$ and $M_p \geq 0.1 M_J$. Planets with $R_p < 10R_{\text{acc}}$ are excluded, but this affects only a small fraction of the points; for example, planets with $M_p \approx 0.1 M_J$ and with a small Hill sphere might be in the attached phase even at high \dot{M} . Essentially all points above $0.5 M_J$ have $R_p > 10R_{\text{acc}}$. Thus, v_0 is indeed given by Equation (7) to 5% or better.

Figure 4a shows that typical preshock velocities are $v_0 \approx 50\text{--}200 \text{ km s}^{-1}$, and that there is a maximal $v_0 \approx 170 \text{ km s}^{-1}$ for masses between $M_p \approx 13$ and $\approx 35 M_J$. (For the hot population, it is also $v_0 \approx 170 \text{ km s}^{-1}$ but with a thicker spread of the horizontal portion there, down to $v_0 \approx 150 \text{ km s}^{-1}$.) The points along this locus of approximately constant v_0 (which implies that $M_p \propto R_p$ approximately) are objects which have not yet burned their deuterium and are all younger than 10 Myr. These points span a range of ages and masses. Thus their distribution is different from the D-burning “shoulder” in plots of the radius of an object of a given mass as a function of time, in which the D burning stalls the cooling (e.g., Mollière & Mordasini 2012, and references therein). Also, these points with $M_p \propto R_p$ are not in conflict with the classical result $M \propto R^{-1/3}$ in that mass regime (Zapolsky & Salpeter 1969) since that holds for “zero-temperature” (i.e., degenerate) objects, whereas the objects here are still forming and thus hotter, also in the sense of not being completely

degenerate. Older, post-deuterium-burning objects have a smaller radius and thus a higher v_0 but they are not plotted because of the selection on \dot{M} . This group of constant- v_0 points could show up as a pile-up in a histogram of v_0 for forming planets.

Figure 4a compares preshock velocities and object radii to young stellar objects (YSOs). As an example, the properties of some of the targets in the Alcalá et al. (2017) sample are shown (crosses), which covers $M \approx 10\text{--}180 M_J$ and $R \approx 2\text{--}30 R_J$, with a preshock velocity $v_{\text{ff}} \approx 150\text{--}500 \text{ km s}^{-1}$. There is no significant overlap between the region occupied by planets and the Alcalá et al. (2017) sample.

Next, Figure 4b situates the planet accretion shock in the input parameter space of preshock velocity v_0 and hydrogen proton density n_0 . The latter is in the range $n_0 = 10^{10}\text{--}10^{14} \text{ cm}^{-3}$, which corresponds to $\rho_0 \sim 10^{-14}\text{--}10^{-10} \text{ g cm}^{-3}$.

We also indicate the preshock state (molecular, atomic, or ionic) of the hydrogen in Figure 4b. We calculate the mean molecular weight μ_0 from ρ_0 and T_0 (x axis and Equation (19), respectively) and the Saha equation. For $f_{\text{fill}} = 1$, the incoming hydrogen is molecular at low densities or velocities and atomic above this. In a few high-velocity cases, it arrives at the shock significantly ionized (bright red points). Overall, according to the (\dot{M}, M_p, R_p) combinations found in the Bern population synthesis, for large filling factors $f_{\text{fill}} \approx 1$ the gas reaches the planet in an atomic form in the majority of cases. Below $v_0 \approx 30 \text{ km s}^{-1}$, the hydrogen is usually molecular, so that there will be no line emission ($H\alpha$, $H\beta$, etc.) because the

shock energy is used up to dissociate the molecules (Aoyama et al. 2018). However, for the cases where the preshock gas is atomic, there is no v_0 emission threshold and the H α flux continuously gets weaker with decreasing v_0 . This is relevant only for a few points. The limit of $v_0 = 30 \text{ km s}^{-1}$ is indicated by the gray areas in Figure 4a and b, with the slanted right edge drawn approximately in panel b.

Finally, we note in passing that the minimum velocity for H α of $v_0 \approx 30 \text{ km s}^{-1}$ puts a constraint on the CPD size needed to have H α in the CPD-shock case studied in Aoyama et al. (2018). Figure 4 shows that if the inner edge of the CPD is further out than 3–5 (7–15) planetary radii for 2–(5)- M_J planets, there will not be any H α emission. For his fiducial values, Batygin (2018) found that the magnetospheric truncation radius $R_{\text{trunc}} \approx 2R_p$. Thus the requirement $v_0 > 30 \text{ km s}^{-1}$ should be easy to meet already at a few M_J and all the more for higher masses. This implies that the CPD could be an emitter of H α . We discuss how to distinguish the emission from a CPD from the one from the planet surface in Section 5.2.

Figure 5 displays contours of n_0 and v_0 in the \dot{M} – M_p plane using the $R_p(\dot{M}, M_p)$ fit (Equation (1)) for the warm and the cold population. (The inverse relations are shown in Figure 14.) We use $f_{\text{fill}} = 1$. The v_0 contours depend on \dot{M} because of the dependence of the radius on \dot{M} . This leads even to a non-monotonic behaviour of v_0 with \dot{M} , with, in the warm (cold) population, a maximum around $\dot{M} \approx 3 \times 10^{-5} M_E \text{ yr}^{-1}$ ($\dot{M} \approx 10^{-3} M_E \text{ yr}^{-1}$). The maximum preshock velocity is for both populations roughly $v_0 \approx 100 \text{ km s}^{-1}$ ($v_0 = 180 \text{ km s}^{-1}$) for $M_p \approx 5$ ($M_p \approx 15\text{--}20 M_J$). Since the radii are smaller in the cold population, the velocities are slightly higher at a given mass but only by some tens of kilometers per second. The curving of the v_0 contours at high v_0 (see Figure 5) means that a measurement of the preshock velocity v_0 , for instance through the Doppler broadening of the emission lines, can be explained only by a limited range of accretion rates, assuming that a rough upper limit on the mass exists (e.g. from imaging or dynamical arguments).

2.2.2. Shock conditions

We assume that at the shock, the preheated gas (Marleau et al. 2019) undergoes a hydrodynamical shock before cooling down radiatively. This corresponds effectively to the Zel’dovich spike (see Vaytet et al. 2013), and our actual computations begin directly after the hydrodynamical shock, i.e., roughly at the tip of the Zel’dovich spike. To obtain this immediate postshock state, we use the classical Rankine–Hugoniot shock jump conditions, which reflect mass, momentum, and energy conservation. This is valid because the time needed for the gas to cross the hydrodynamical shock thickness, of the order of a particle mean free path, is much less than the cooling timescale of the gas. In Marleau et al. (2017, 2019),

“the shock” referred to both the hydrodynamic jump and the postshock cooling region; here we refer by “shock” only to the hydrodynamic jump, with the postshock cooling region the focus of this work. The Rankine–Hugoniot relations read:

$$\rho_1 = \frac{(\gamma + 1)\mathcal{M}^2}{(\gamma - 1)\mathcal{M}^2 + 2}\rho_0 \quad (10)$$

$$v_1 = \frac{\rho_0 v_0}{\rho_1} \quad (11)$$

$$P_1 = \frac{2\gamma\mathcal{M}^2 - (\gamma - 1)}{\gamma + 1}P_0 \quad (12)$$

$$= \frac{2}{\gamma + 1}P_{\text{ram}} - \frac{\gamma - 1}{\gamma + 1}P_0, \quad (13)$$

with the subscript “0” denoting the preshock and “1” the postshock state. The ram pressure is $P_{\text{ram}} \equiv \rho_0 v_0^2$. The upstream Mach number is $\mathcal{M} = v_0/c_s$, with $c_s = \sqrt{\Gamma_{1,0}k_B T_0/(\mu_0 m_H)}$, where $\Gamma_1 = (\partial \ln P/\partial \ln \rho)_s$ is the first adiabatic index and s the entropy. Across the hydrodynamic jump (but not below, in the main part of our computations), we assume that the abundances and thus μ and Γ_1 remain constant. This is justified if the gas undergoes the jump (a few mean free paths thick) on a timescale shorter than the chemical reaction time. For simplicity, we take $\Gamma_1 = \gamma$, where γ is the ratio of specific heats, and we specify its value below (see Equation (20)). The high-Mach number limits for ρ_1 and P_1 are

$$\rho_1 = \frac{\gamma + 1}{\gamma - 1}\rho_0 \quad (14)$$

$$P_1 = \frac{2\gamma\mathcal{M}^2}{\gamma + 1}P_0 \quad (15)$$

$$= \frac{2}{\gamma + 1}P_{\text{ram}}, \quad (16)$$

which implies, still in the limit $\mathcal{M} \gg 1$,

$$T_1 = \frac{\mu_0 m_H}{k_B} \frac{2(\gamma - 1)}{(\gamma + 1)^2} v_0^2 \quad (17)$$

$$\approx 4 \times 10^5 \left(\frac{M_p}{10 M_J} \right) \left(\frac{2 R_J}{R_p} \right) \text{ K}, \quad (18)$$

taking $\mu = 1.23$ and $\gamma = 1.43$ (generally appropriate for the incoming gas; see Figure 4) for the second line. Expressions for the case of different γ and μ values left and right of the shock can be found in Equation (4.17ff) of Drake (2006). This is the same physics as for stars (see Equation (4) of Hartmann et al. 2016). Note that T_1 is a *non-equilibrium* temperature, which holds over only a very small temporal and spatial scale relative to any other relevant scale. (In the example in Figure 6, this is $\sim 10^{-2} \text{ s}$ and $\sim 10^{-6} R_J$.) It is thus in no way an effective temperature T_{eff} nor an equilibrium gas temperature. This non-LTE effect usually cannot be resolved in full radiation-hydrodynamical simulations because of the vast differences in scales.

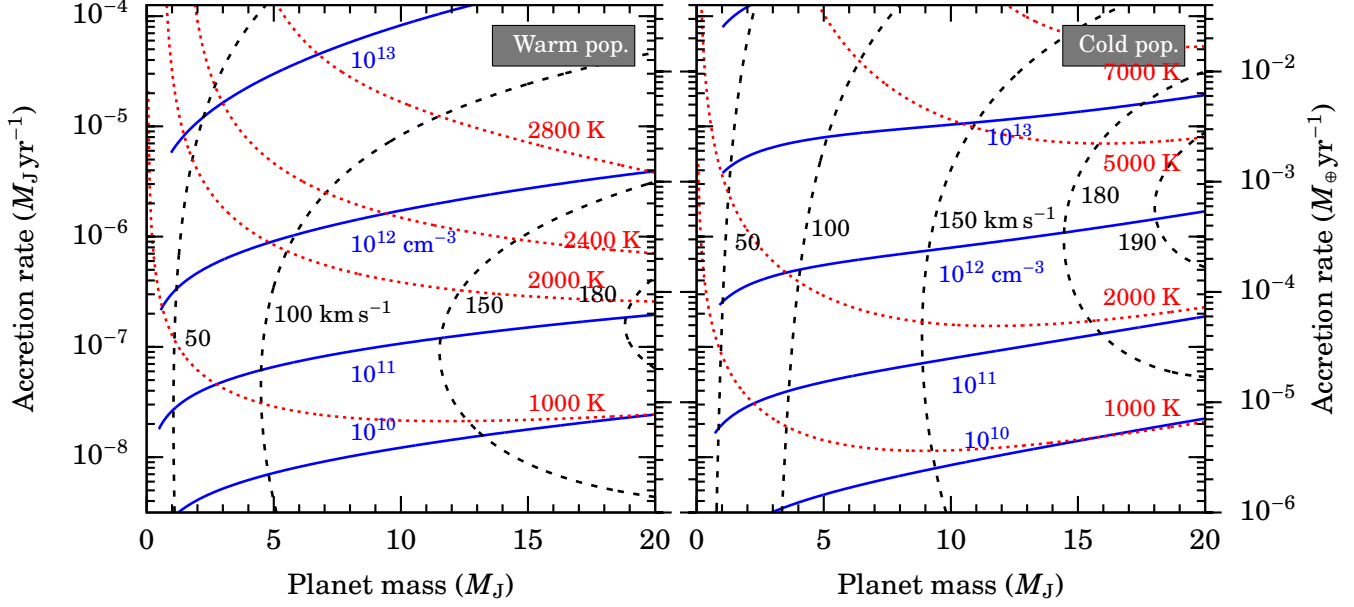


Figure 5. Contours of $n_0 = 10^{10}$ – 10^{14} cm^{-3} (blue solid lines), $v_0 = 50$ – 190 km s^{-1} (black dashed), and $T_0 = 1000$ – 7000 K (red dotted) from Equations (7)–(8) and (19) in the mass–accretion rate plane. We set $f_{\text{fill}} = 1$ and use the radius fitted to the population synthesis results in the warm (left panel) and cold (right panel) cases. The highest v_0 , n_0 , and T_0 contours are missing in the warm population due to the larger radii. The inverse relations are shown in Figure 14. Note that $1 M_J \text{ yr}^{-1} \approx 3 \times 10^{-4} M_{\odot} \text{ yr}^{-1}$.

The preshock temperature T_0 is needed to set the preshock pressure P_0 and the preshock Mach number \mathcal{M} , as well as the chemical abundances before and therefore also directly below the shock. Using gray radiation transfer, Marleau et al. (2017, 2019) found that the radiation and the gas ahead of the shock were able to equilibrate. This is due to the sufficiently high Planck opacity of the gas or, for lower shock temperatures, of the dust. Therefore, we calculate the preshock temperature from (ρ_0, v_0) by

$$T_0 = \sqrt[4]{\frac{\rho_0 v_0^3}{2\sigma}}. \quad (19)$$

Because it has σ and not $ac = 4\sigma$ on the denominator, where a is the radiation constant and c the speed of light, this expression is higher by a factor of $4^{1/4} \approx 1.4$ than the equilibrium shock temperature obtained analytically and numerically by Marleau et al. (2019, see their Equation (6))⁶. It also ignores the negligible contribution of the internal luminosity in setting the planet’s surface temperature; see e.g. Equation (32) of Marleau et al. (2019). However, since the shock is strong (i.e., the Mach number is large; Marleau et al. 2019), both \mathcal{M} and P_0 barely affect the postshock quantities, as Equations (14) and (16) show. Thus it is inconsequential that Aoyama et al. (2018) assumed a constant $T_0 = 200$ K. Also,

⁶ We noticed this difference only at a later stage of this work. Since it barely changes the results, a correction of this factor will be deferred to the next iteration of our models.

the initial postshock composition does not affect the radiative fluxes by more than $\sim 1\%$, as we have verified (not shown) by varying T_0 even by a factor of ten.

Finally, the adiabatic index for the mixture is given by

$$\frac{1}{\gamma - 1} = \sum \frac{y_i/y_t}{\gamma_i - 1}, \quad (20)$$

with $\gamma = 5/3$ for H, He, C, and O, and $\gamma = 7/5$ for H_2 . It enters into the Rankine–Hugoniot equations and in the time-dependent energy equation through $P = (\gamma - 1)E$, where P is the pressure and E the internal energy (see Equation (7) of Aoyama et al. (2018)).

2.2.3. Postshock flow

We assume a time-independent plane-parallel one-dimensional flow after the shock. Then, the gas flows with conserved mass flux and momentum flux, implying

$$\rho v = \rho_1 v_1 \quad (21)$$

$$\rho v^2 + P = \rho_1 v_1^2 + P_1. \quad (22)$$

Chemical reactions including electron level transitions are the external energy source. Therefore, the internal-energy volume density of the gas E is not conserved but evolves according to

$$\frac{dE}{dt} = (\Gamma - \Lambda) + \left[\frac{P + E}{\rho} \frac{d\rho}{dt} \right], \quad (23)$$

where Γ and Λ are the heating and cooling rates per unit volume, respectively. Note that, in a 1-D flow, temporal differentiation is easily converted into spatial differentiation with flow velocity v .

In this study, the coolants are the dissociation of molecular hydrogen, the collisional excitation and ionization of atomic hydrogen, and the emission of radiation by CO, OH, and H₂O. The heat sources are the formation of molecular hydrogen as well as the collisional de-excitation and collisional recombination of atomic hydrogen. For detailed expressions, see [Aoyama et al. \(2018\)](#).

2.2.4. Radiative transfer

We consider electron level transitions between ten levels of neutral hydrogen and the ionized state. We numerically calculate the radiative transfer of 45 lines and ten recombination continua with de-exciting transitions. To integrate the flux, we use the two-stream approximation, assuming a plane-parallel 1-D flow. We iterated the hydrodynamic simulation and the radiative transfer until the H α flux converges. Note that since the Ly α still changes when the other lines converge and the iteration stops, the Ly α intensity is less reliable, in this model. Detailed expression and equations are given in [Aoyama et al. \(2018\)](#).

Finally, given the assumed geometry described in Section 2.2.1, the luminosity of hydrogen lines and recombination continua emitted from the shock-heated gas is

$$L = 4\pi R_p^2 f_{\text{fill}} F, \quad (24)$$

where F is the photon energy flux at the shock and is the result of the radiative transfer in the postshock gas flow.

2.3. Neglecting extinction

In this work, extinction by material between the shock surface (the planet) and the observer is not considered. Several components contribute to it. In principle, the contribution from the interstellar medium (ISM) can be determined for a given source, from the stellar spectrum or by statistical tools such as *Stilism* of [Lallement et al. \(2019\)](#). Thus this component is relatively easily accounted for. To what extent the gas or dust surrounding a forming planet may weaken the shock signal is an important question, as the recent observational results and theoretical modeling in [Hashimoto et al. \(2020\)](#), [Stolker et al. \(2020a\)](#), and [Sanchis et al. \(2020\)](#) highlight. However, considering extinction adds an entire level of complexity and brings many uncertainties, in particular concerning the radiative transfer geometry and the dust opacity. Therefore, we deal with extinction by the gas and the dust in a dedicated paper ([Marleau et al. *in press*](#)).

Nevertheless, the extinction-free case is relevant in itself. As we show in [Marleau et al. \(*in press*\)](#), an accretion flow free of extinction at H α is a plausible assumption for a wide range

of accretion rates and masses. We look at this in detail but, heuristically, the transition disk gaps in which planets are found are usually dust-free ([Close 2020](#)), and gas cooler than a few thousand kelvin can be optically thin for non-Lyman-series hydrogen lines. Also, while [Hashimoto et al. \(2020\)](#) derived for PDS 70 b an extinction of > 2.0 mag at H α , we should recall that this is for a single object (PDS 70 b), and that this estimate depends on the wide spectral width of the observed H α line (see Section 4.1), which can be overestimated due to the finite instrumental resolution ([Thanathibodee et al. 2019](#)). More generally, it is conceivable that for some accretion and viewing geometries the H α produced at the shock could leave the system without passing through any absorbing material that could be present. For these reasons, it seems sensible to treat the extincted case separately.

3. THEORETICAL SPECTRA OF FORMING GAS GIANTS

We now turn to results from the methods described above. We look first at one representative example in detail (Section 3.1; [Aoyama et al. 2018](#) showed three other cases for the CPD case) and then survey a large part of the relevant (\dot{M} , M_p) parameter space (Section 3.2).

3.1. One example

3.1.1. Postshock structure

The postshock structure and hydrogen line emission were detailed by [Aoyama et al. \(2018\)](#). Although the results shown here are basically the same as theirs, we review their findings in this subsection for the reader's convenience. Also, the input parameters are chosen to be appropriate for the detected planet PDS 70 b. The v_0 and n_0 are higher than in [Aoyama et al. \(2018\)](#), where we focused on the CPD surface shock rather than the planetary surface.

In Figure 6 we show one example of the postshock structure for $v_0 = 100$ km s⁻¹ and $n_0 = 10^{11}$ cm⁻³. This corresponds to, for example, $\dot{M} = 10^{-8} M_J$ yr⁻¹, $M_p = 5 M_J$, and $R_p = 1.7 R_J$ with $f_{\text{fill}} = 1$, assuming the radius fit to the warm population (see Figure 4 and Section 2.1.1). Following Equation (19), the preshock temperature is $T_0 \approx 1200$ K, and with $\rho_0 = 2.3 \times 10^{-13}$ g cm⁻³ this implies $\mu = 2.3$ and $\mathcal{M} \approx 45$. The hydrodynamic shock heats the gas to $T_1 \approx 4 \times 10^5$ K (panel (a)). The gas density (not shown) increases as the temperature drops. Although the gas cools, the gas pressure increases slightly, by only 30% at the end of this simulation, because of the density enhancement of compression. Notice that the pressure gets low once around the depth of 2×10^3 cm (10^{-3} s) because H₂ dissociation results in expansion.

Immediately after the shock, the dissociation of H₂ is the main process responsible for the cooling of the gas. However, it can bring down the temperature only by a small amount before the collisional excitation of the atomic hydrogen and

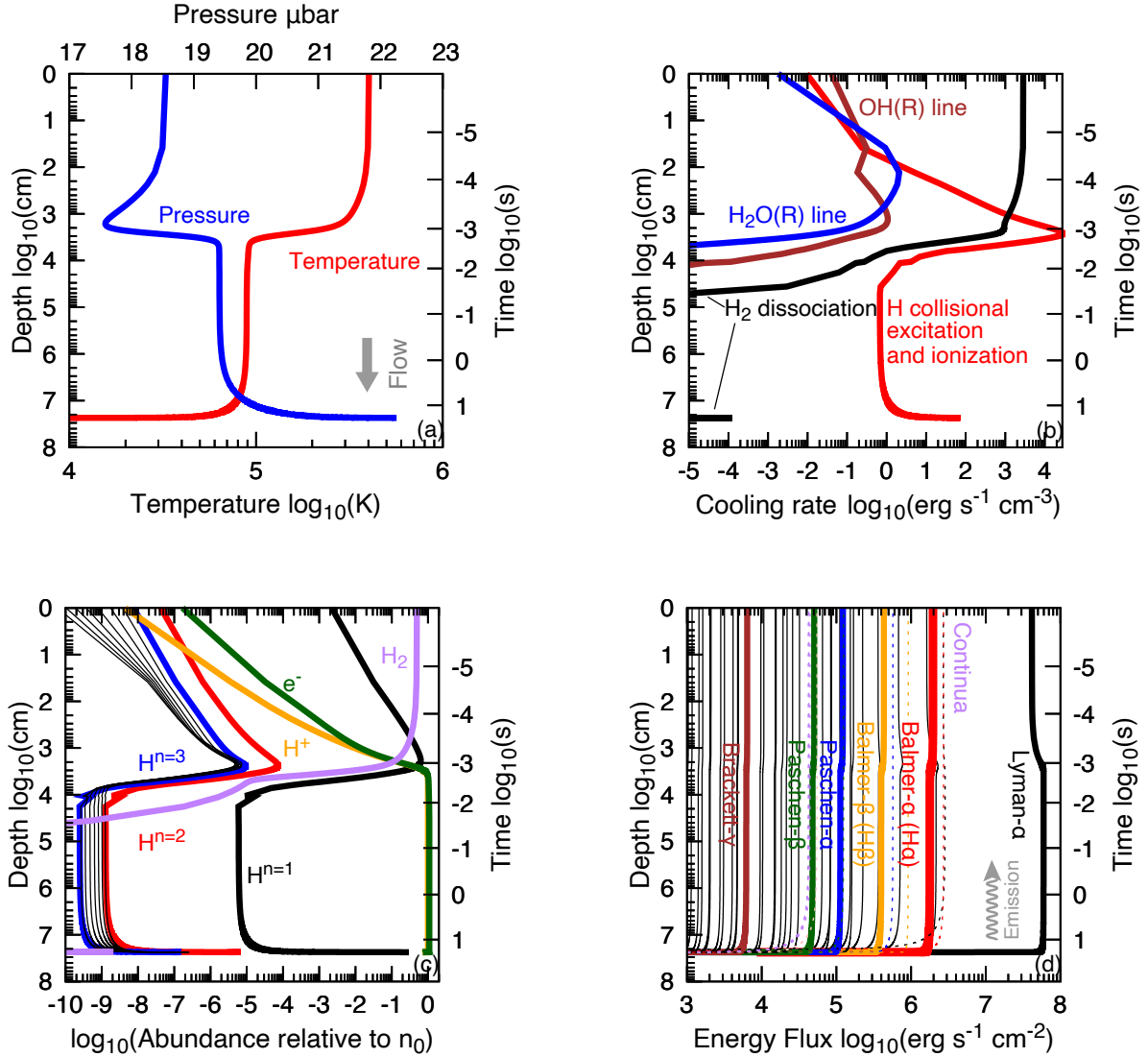


Figure 6. Postshock flow structure, beginning immediately after the hydrodynamical jump, for $v_0 = 100 \text{ km s}^{-1}$ and $n_0 = 10^{11} \text{ cm}^{-3}$. This corresponds for example to $\dot{M} = 10^{-8} M_J \text{ yr}^{-1}$, $M_p = 5 M_J$, and $R_p = 1.7 R_J$ with $f_{\text{fill}} = 1$. The left (right) axes are the depth below (time elapsed after) the shock surface Δz (Δt). (a): Temperature T (red line, bottom axis) and pressure P (blue line, top linear axis). The preshock T (not shown) is $T_0 \approx 1190 \text{ K}$. The P profile changes inversely to T because the density increases faster than T drops. (b): Cooling rates of H collisional excitation and ionization (red line), dissociation of H₂ (black), and OH (brown) and H₂O (blue) rotational line emission. Throughout the simulation, molecules hardly affect the cooling because they are minor relative to neutral hydrogen. (c): Number density relative to n_0 (see Section 2.2.1) for H₂ (purple), H ^{$n=1$} (black), H ^{$n=2$} (red), H ^{$n=3$} (blue), H⁺ (orange), and e⁻ (green), with n the principal quantum number. Thin black lines show $n \geq 4$ states. At intermediate depths, the H ionization fraction approaches unity. (d): Upward energy flux of Ly α (black line), Ba α (H α ; red), Pa α (blue), Pa β (green), Br γ (brown), recombination continua (thin dotted; Lyman (black), Balmer (red), Paschen (blue), Blackett (orange), Pfund (green), Humphreys (pink), and others (purple)), and other lines (thin black)). At intermediate depths, the line fluxes hardly change due to the optical thinness of the gas. The deep region in which the fluxes originate is well resolved by steps of 10% in T , but the details are not seen easily due to the logarithmic scale.

its ionization take over some $\Delta t \sim 10^{-3}$ s after the shock (Figure 6b). The excitation and dissociation dominate until the end of the simulation when T reaches 10^4 K. Throughout the simulation, molecules hardly affect the cooling because they are minor relative to neutral hydrogen.

Figure 6c shows the abundance of each form of hydrogen relative to all hydrogen protons. At the preshock temperature $T_0 \approx 1200$ K and thus at the beginning of the evolution in the postshock region, the molecular form H_2 (purple curve) is the most abundant, orders of magnitude more so than the ground state of atomic hydrogen $H^{n=1}$ (black) or ionized hydrogen H^+ (dark yellow). This is why immediately after the shock hydrogen dissociation is the most important process. Near $\Delta t \approx 10^{-3}$ s, neutral hydrogen dominates, but very quickly, by $\Delta t \approx 2 \times 10^{-3}$ s ($\Delta z \approx 5000$ cm), the ionization fraction has nearly reached unity. Excitation from the ground state to the first excited state $n = 2$ nevertheless proceeds simultaneously. The main processes increasing and decreasing the $n = 3$ population is collisional excitation from $n \leq 2$ to $n = 3$ and radiative de-excitation from $n = 3$ to $n < 3$. The $n = 2$ level is special because Ly α ($n = 2 \rightarrow 1$) is optically thick at this location in this example, which prevents radiative de-excitation. If the gas were even denser, also H α would become optically thick, which would prevent radiative de-excitation and lead to a higher $n = 3$ population. At depths $\Delta z \gtrsim 1 \times 10^7$ cm, the dropping temperature and the longer timescale let the hydrogen recombine and the electrons fall back down to lower levels.

As Figure 6d reveals, the (potentially observable) hydrogen lines originate mainly in the deepest part, at $\Delta z \approx 2 \times 10^7$ cm (or $\Delta t \approx 30$ s), from the de-excitation of the electrons. This region seems narrow on a logarithmic scale but we recall that the adaptive step size in time or space is set by a temperature criterion, ensuring sufficient resolution (Aoyama et al. 2018). Above this region, i.e., for most of the postshock flow as visible in Figure 6, the line fluxes remain approximately constant, with only small modulations that can be related to the cooling processes shown in panel (b). In general, to zeroth order, when the gas is optically thin and all the energy is in hydrogen lines, a half goes outward as Ly α and the other half goes inward also as Ly α . In this example, at the shock surface, the upward-travelling Lyman- α flux represents around 76 % of the incoming (mostly kinetic) energy, and H α carries only around 1 %. The other part of the energy influx travels downward, towards the photosphere (see also Section 2.1.2 for more precise fractions).

In our models, we currently do not include cooling from He or metal lines but this ultimately does not matter. In most regions, hydrogen lines are almost the only coolant, so that when the abundance of neutral hydrogen becomes low enough, cooling by hydrogen becomes inefficient. In Figure 6, this is between $\Delta z \approx 8 \times 10^3$ and 5×10^7 cm. This

leads to a plateau in the temperature, which ends where the hydrogen recombines. In that temperature region (at $T \sim 10^5$ K), cooling by lines of ionic C, O, and He (specifically, the He $\lambda 16404$ line) or other metals lines would be more important (see Figure 3 in Gnat & Ferland 2012) so that there would not be a temperature plateau. Indeed, while the ionisation of C and O is included in the chemistry subroutine, it is not included in the radiation transfer, and neither is the cooling by lines of C and O in the energy equation. For helium, the ionisation is included in the energy equation but, also here, the lines are not. Also, note that for the case presented in Figure 2 of Aoyama et al. (2018), with ($v_0 = 40$ km s $^{-1}$, $n_0 = 10^{11}$ cm $^{-3}$), in the early parts of the flow the electron abundance is higher than the H^+ abundance. These electrons are coming from ionized helium.

However, the gas in the region of the temperature plateau only contributes to the recombination continuum but not to the hydrogen lines. Therefore, even including helium or metal lines (and thus changing the temperature structure of that region) would not modify the strength of the hydrogen lines.

3.1.2. Radiative properties

Figure 7 shows the entire corresponding SED, including the contribution from the photosphere. For optical or longer wavelengths ($\lambda \gtrsim 4000$ Å), the radiation is dominated by the photospheric contribution (black line) except for some hydrogen lines (red peaks). On the other hand, at shorter wavelength, the dominant component is Ly α , stronger by tens of orders of magnitude than the thermal photospheric emission. The other Lyman and Balmer line series also clearly exceed the photospheric contribution. Notice also the clearly visible Lyman and Balmer recombination continua. These are the smooth parts of the SED between roughly 500 and 900 Å (with 921 Å the edge of our Lyman continuum at $n > 10$ instead of 912 Å for $n = \infty$) and 1000 and 4000 Å, respectively. The continua for the other series are hidden by the photospheric contribution and are thus negligible. Some of the integrated continua fluxes exceed some of the line-integrated fluxes (the details depend strongly on the input parameters) but the lines are obviously narrower than the continua; thus the lines are not necessarily embedded in the recombination continua. In any case, as we discuss in Section 6.3, the strength and shape of the continua are approximate—within a factor of a few, but also possibly exceeding this—and are only meant to provide some guidance. Also, note that the continua (hydrogen recombination and H^-) are thought to mainly come from the deeper and cooler region (heated photosphere after (or under) the end of our calculation).

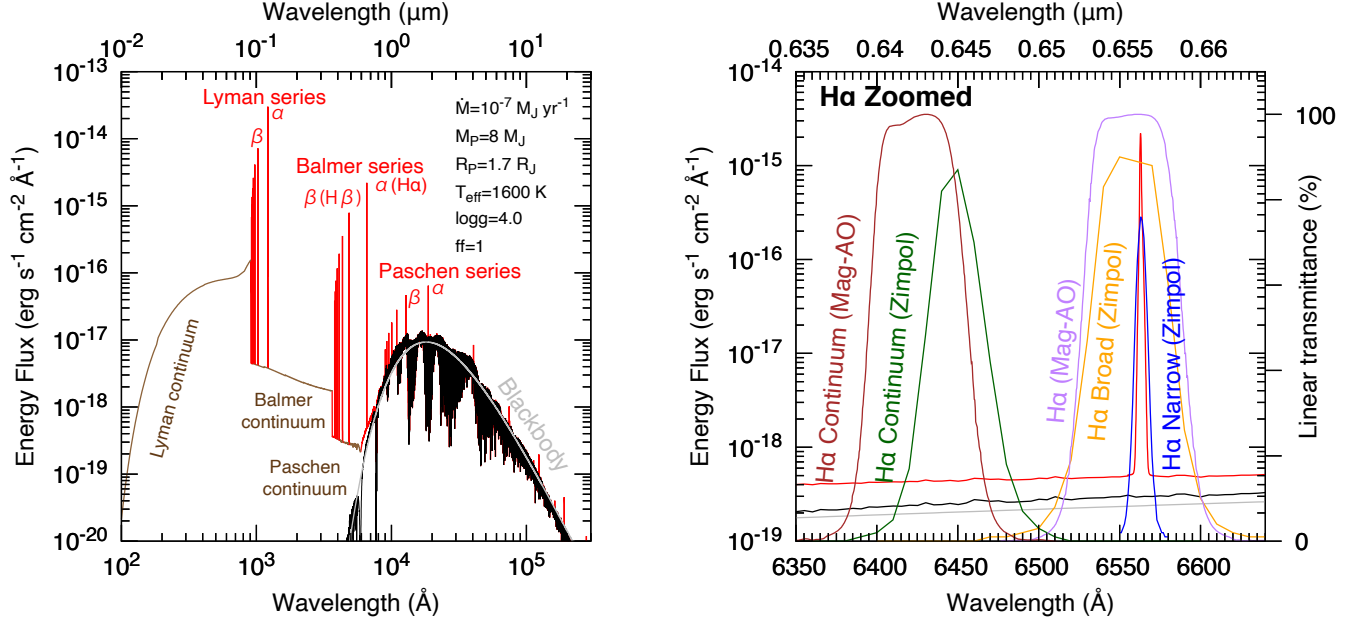


Figure 7. Spectral energy distribution of an accreting gas giant, with effective temperature $T_{\text{eff}} = 1600$ K and surface gravity $\log g = 4.0$ (cm s^{-2}). This corresponds for example to a $M_p = 8 M_J$ planet accreting at $\dot{M} = 10^{-7} M_J \text{ yr}^{-1}$ with $f_{\text{fill}} = 1$ in the hot-start population. The energy flux is for a distance of 150 pc to the system. The black line shows the pure photospheric radiation (BT-Settl; Allard et al. 2012) and the red shows the photospheric radiation with the shock excess. The pale gray line is a blackbody at $T_{\text{eff}} = 1600$ K. *Left panel:* Global SED. The continua are plotted darker to indicate that they are less certain. Only the Lyman, Balmer, and Paschen continua are brighter than the photosphere. *Right panel:* Zoom-in on the $H\alpha$ region, showing (right axis) the transmittance of the SPHERE/ZIMPOL $H\alpha$ Continuum (green), $H\alpha$ Broad (yellow), and $H\alpha$ Narrow (blue) filters (Schmid et al. 2018; see Footnote 7), as well as the MagAO $H\alpha$ filter, normalised to 100%. The red peak near 6560 \AA is the $H\alpha$ line from the shock. The blackbody is visible as the nearly flat gray line.

In the right panel of Figure 7, we zoom in onto the $H\alpha$ region and compare with the SPHERE/ZIMPOL $H\alpha$ filters⁷ (Schmid et al. 2018) and also show the MagAO filter⁸. In this panel, an atmospheric reflective index of 1.000276 (Ciddor 1996) is assumed for matching the line and filter peaks. The $H\alpha$ line is narrower than filters, i.e., unresolved in all. Therefore, clearly, the high-resolution line profiles shown in Aoyama et al. (2018) and Aoyama & Ikoma (2019) cannot be resolved even with narrow-band filters. Nevertheless, the line in Figure 7b contributes around 99% of the flux in the SPHERE Narrow filter but also in the broad filters (SPHERE or MagAO), clearly dominating over the contribution from the heated photosphere. Also, we note that the narrow filter well contains most of the $H\alpha$ flux even after taking the spec-

tral shifts into account. By design, the continuum filters are securely distant from the $H\alpha$ line.

3.2. Grid of models

We now present results from a large grid in accretion rate and mass,

$$10^{-8} M_J \text{ yr}^{-1} \lesssim \dot{M} \lesssim 10^{-4} M_J \text{ yr}^{-1} \quad (25)$$

$$0.5 M_J \lesssim M_p \lesssim 20 M_J. \quad (26)$$

This wide parameter space is chosen to cover present and future observations, which might reveal a population of closer-in accreting planets (Close 2020). The $R_p(\dot{M}, M_p)$ and $T_{\text{eff}}(\dot{M}, M_p)$ are given by the relations of Section 2.1, where T_{eff} is chosen so that the total flux in the SED is equal to the sum of the internal and the incoming kinetic energy flux (Equation (5)). We take as the standard case the radius fit from the “accretion hot-start” population and set $f_{\text{fill}} = 1$ for simplicity.

The upper accretion rate of $\dot{M} \approx 10^{-4} M_J \text{ yr}^{-1}$ represents the highest values in the runaway phase (Phase II) of classical in formation calculations, with a dependence on the viscosity and the scale height of the PPD, as reviewed in Helled et al. (2014). Included within this bound are thus the common maximum values near $10^{-2} M_E \text{ yr}^{-1} \approx 10^{-4.5} M_J \text{ yr}^{-1}$

⁷ These smooth curves are from J. Milli (2019, priv. comm.); lower-resolution filters are available at <https://www.eso.org/sci/facilities/paranal/instruments/sphere/inst/filters.html>. Note that in Table 6 of Schmid et al. (2018) there is a typographical error: the central wavelength of the $H\alpha$ filters should read not 656.9 nm but rather $\lambda_c = 656.3$ or 656.5 nm as in Table 5 of Schmid et al. (2017) (H.-M. Schmid 2020, priv. comm.).

⁸ See “VisAO Filters” under https://xwcl.science/magao/visao/group_reduction_users_guide.html.

(Bodenheimer et al. 2000; Marley et al. 2007; Lissauer et al. 2009; Mordasini et al. 2012a; Tanigawa & Tanaka 2016; see also Schulik et al. 2020) so that our upper value represents a conservative choice. It also equals the typical accretion rate through the PPD $\dot{M}_{\text{disk}} \sim 10^{-8} M_{\odot} \text{yr}^{-1}$ (Hartmann et al. 2016); the planet would be intercepting the full typical \dot{M}_{disk} or a smaller fraction of a higher global value.

The smallest $\dot{M} = 10^{-8} M_{\text{J}} \text{yr}^{-1}$ will turn out to be roughly the lower limit needed to explain the PDS 70 b and c observations of Haffert et al. (2019). Also, towards low \dot{M} we expect the photospheric noise to dominate over the accretion lines, in addition to the total line luminosity becoming small, making it a less interesting case to study.

The lower mass of $M_{\text{p}} = 0.5 M_{\text{J}}$ corresponds to a free-fall velocity near 30 km s^{-1} (see Figure 4), which is the lower limit on v_0 for hydrogen line emission when the preshock gas is in molecular form (Aoyama et al. 2018). As discussed in Section 2.2.1, it is not certain at these masses $\lesssim M_{\text{J}}$ to what extent the accreting gas is indeed in free-fall, and the preshock velocity could be smaller. Thus this is an optimistic choice, especially since extinction by the upper layers of the PPD could be important for small masses, which may not carve out a deep gap.

Finally, we take as an upper limit $M_{\text{p}} = 20 M_{\text{J}}$ for a few reasons. One is to focus on objects that are predominantly formed as planets, during the formation of which an accretion shock should occur, whereas this is less clear for brown dwarfs (see discussion in Section 4.2 of Baruteau et al. 2016). The planet and brown-dwarf mass functions overlap⁹ and have a minimum near $M_{\text{p}} = 25 M_{\text{J}}$ (Reggiani et al. 2016) before increasing towards low masses (Nielsen et al. 2019). Thus most objects with $M_{\text{p}} \lesssim 20 M_{\text{J}}$ are likely to have formed by core accretion (Schlaufman 2018; Wagner et al. 2019) and thus to have experienced an accretion shock, making them more observationally relevant. Secondly, we will see that towards higher masses, the line fluxes are relatively insensitive to the mass; thus stopping at 20 or 30 M_{J} makes little difference.

In any case, we emphasise that the range of \dot{M} and M_{p} in Equations (25) is not a prediction but rather meant as a conservative *choice* for the input parameters, that is to say, a generous range of possibly relevant values. We are not making statistical predictions for the $\text{H}\alpha$ luminosities as in Mordasini et al. (2017).

Figure 8 shows a grid of SEDs for $M_{\text{p}}/M_{\text{J}} = 1, 3, 10, 20$ and $\dot{M}/(M_{\text{J}} \text{yr}^{-1}) = 10^{-8}, 10^{-7}, 10^{-6}, 10^{-5}$. The peak intensities of the $\text{H}\alpha$ and other hydrogen lines are significant relative to photospheric emission and increase with v_0 . In all panels except ($\dot{M} = 10^{-5} M_{\text{J}} \text{yr}^{-1}, M_{\text{p}} = 1 M_{\text{J}}$), the $\text{Ly}\alpha$

line at $\lambda = 1215 \text{ \AA}$ has the highest peak value. The effective temperature T_{eff} is almost a monotonic function of both \dot{M} and M_{p} (cf. Section 2.1.2). With increasing planet mass and decreasing accretion rate, the Lyman continuum blueward of $\lambda \approx 912 \text{ \AA}$ becomes stronger relative to the hydrogen lines. As discussed in Section 3.1.1, this means that a large fraction of the hydrogen is ionized and that, in reality, a large fraction of the energy should be converted into He and metal lines instead. However, again, this does not affect the strength of the hydrogen lines.

In all cases shown, Lyman and Balmer lines have significant peaks above the photospheric emission, because the peak of photospheric emission is at a longer wavelength than these lines. Even when we integrated the flux within the SPHERE or Mag-AO broadband filters (not shown), the $\text{H}\alpha$ contribution dominates over the photospheric emission.

Figure 8 also shows that the ratio of the $\text{Ly}\alpha$ to the $\text{H}\alpha$ peaks increases with planet mass, and that for $M_{\text{p}} \approx 1 M_{\text{J}}$, the ratio also increases with decreasing \dot{M} . This is because at high postshock temperatures T_1 (high M_{p} ; see Equation (17)), hydrogen excitation occurs. This increases the abundance of the absorber of $\text{H}\alpha$, namely electrons in the $n = 2$ state, while depopulating the absorber of $\text{Ly}\alpha$, electrons in $n = 1$. This leads to a lower $\text{H}\alpha/\text{Ly}\alpha$ ratio. Towards high postshock densities (high \dot{M} ; see Equation (9)), both $\text{H}\alpha$ and $\text{Ly}\alpha$ are more strongly absorbed. However, this absorption occurs in the upper regions (small Δz), where the temperature is high but the excitation degree is low. Normally, hotter gas emits and cooler gas absorbs, but since the hot gas has a low excitation degree, the hot gas can absorb. This is a non-equilibrium (NLTE) effect not captured by a time-independent approach. Therefore, since the lower levels of hydrogen are more populated, $\text{Ly}\alpha$ absorption is stronger than $\text{H}\alpha$ absorption. This leads to the increase of $\text{H}\alpha/\text{Ly}\alpha$ with \dot{M} .

In Figure 8, we also see that longer-wavelength series (e.g., Paschen or Brackett) are embedded in the photospheric signal but tend to emerge towards larger masses and accretion rates. This suggests that high-resolution spectroscopy of strongly accreting or massive planets might be able to detect lines from these other series (see also Sections 5.3 and 5.4), unless infrared excess from dust particles in CPD is significant enough.

Particularly with the hot-start radii, the Mach number is not monotonically proportional to \dot{M} because of the non-monotonic dependence of \dot{M} on the radius. Although increasing the mass flux of accreting gas \dot{M} increases the amount of shock-heated (and thus emitting) gas, it is associated with a larger planet radius at the same time. In turn, the larger planet radius leads to a slower free-fall velocity at the planet surface v_0 . Figure 8 reflects this, given that, as we verified, the $\text{H}\alpha$ continuum is an at least roughly monotonic function of T_{eff} at fixed planet mass.

⁹Core accretion can form objects up to several tens of M_{J} , with a low frequency (Mordasini et al. 2012a; Emsenhuber et al. 2020b).

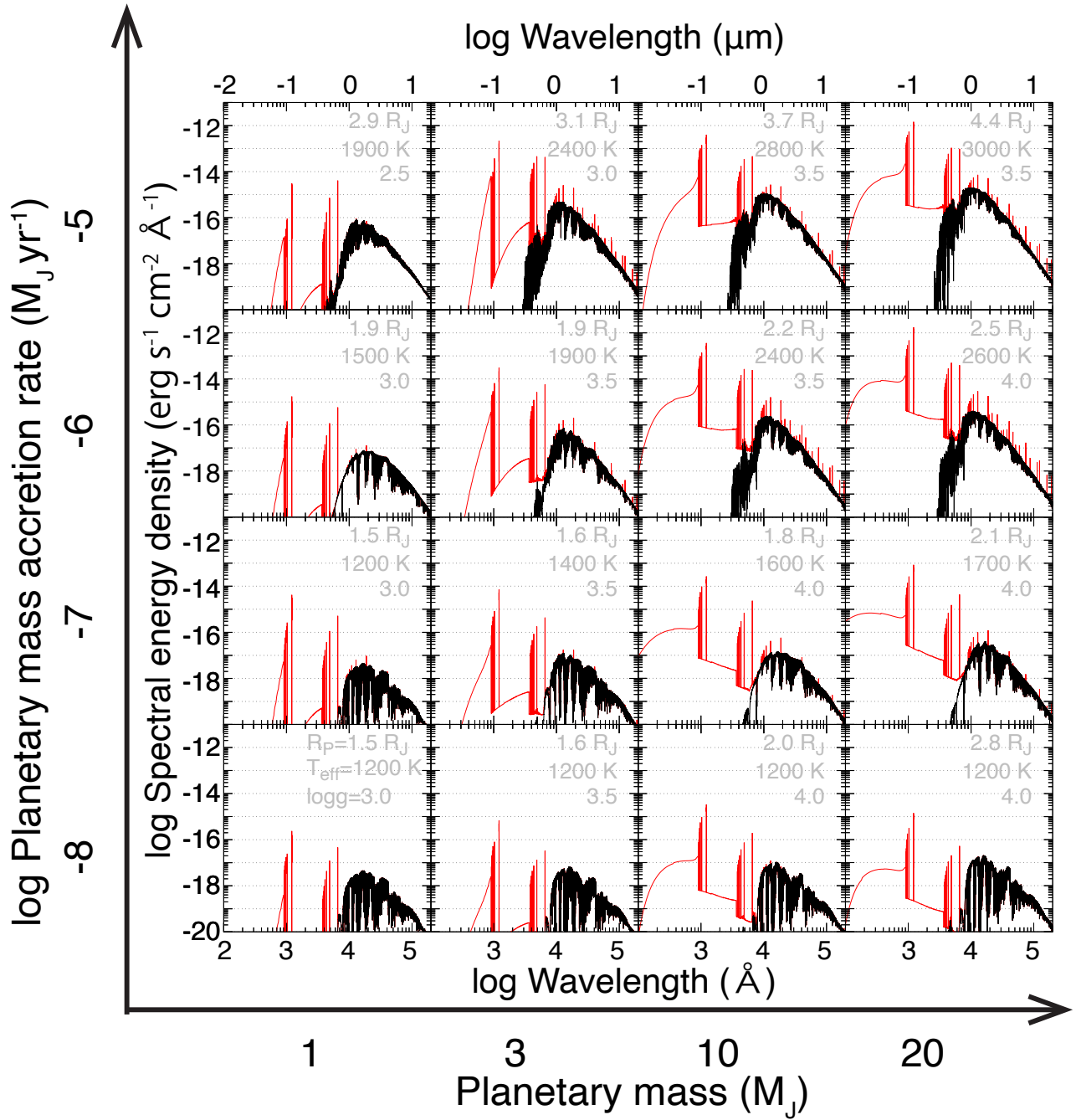


Figure 8. SEDs of accreting planets for a grid of accretion rates and masses: photospheric emission only (black lines) or including the shock-heated gas emission (red). We took $f_{\text{fill}} = 1$, a distance of 150 pc, and the hot-start fits (Section 2.1.1) for the planetary radius R_p and effective temperature T_{eff} (see subpanels), rounded to the nearest 100 K or up to $T_{\text{eff}} = 1200$ K. No CPD contribution (Zhu 2015) is shown.

As one of the most important results of this work, Figure 9 shows the $H\alpha$ line luminosity as a function of \dot{M} and M_p . We extrapolated the model results down to $\dot{M} \sim 10^{-9.5} M_J \text{ yr}^{-1}$. Note that Figure 3 of Aoyama & Ikoma (2019) is similar but was made for a fixed $R_p = 2 R_J$, independently of \dot{M} and M_p . The $H\alpha$ luminosity $L_{H\alpha}$ ranges from $\sim 10^{-9} L_\odot$ to $\sim 10^{-3} L_\odot$ over the grid, overall increasing monotonically with both \dot{M} and M_p . The contours show that for $M_p \gtrsim 3\text{--}5 M_J$, the $H\alpha$ luminosity is independent of M_p and is roughly linearly proportional to \dot{M} . The first part of the reason for this is that the $H\alpha$ luminosity turns out to be roughly linearly proportional to the incoming kinetic energy flux $L_{\text{acc}} = GM_p \dot{M} / R_p$ (Aoyama et al. 2018), especially at a fixed mass (see Figure 2 in Section 2.1.2). The second part is a simple one: the mass coordinate is on a linear scale, with only a limited range (≈ 1.3 dex) relevant to planetary detections, while the accretion rate axis is logarithmic and chosen to cover five orders of magnitude.

Our $L_{H\alpha}(\dot{M}, M_p)$ relation (Figure 9) is robust to changes in the model choices. We compare in Appendix C the luminosity as obtained with the hot- and the cold-start R_p and T_{eff} relationships and find very little difference. Similarly, varying f_{fill} from $f_{\text{fill}} = 1$ to $f_{\text{fill}} = 0.01$ (not shown) changes the $H\alpha$ fluxes by at most a factor of two¹⁰. This is because the incoming gas mass at the shock (\dot{M}) is independent of f_{fill} , and $H\alpha$ emission is almost proportional to the mechanical energy of incoming gas (Aoyama et al. 2018), as mentioned above. See also the discussion in Section 6.2.

Figure 9 is meant as a tool for interpreting $H\alpha$ detections in terms of fundamental planet parameters. Therefore, we also compare the luminosities with those of a few low-mass objects (labeled contours), which we discuss in the next section. Section 5.3 presents the Br γ , Pa α , Pa β , and H β luminosities in a similar fashion.

4. APPLICATION TO OBSERVATIONS

In this section, we apply our results to a few (candidate) protoplanets¹¹. Implications of the non-detections in dedicated surveys (Cugno et al. 2019; Zurlo et al. 2020; Xie et al. 2020) are discussed in Sections 6.5.

4.1. PDS 70 b and PDS 70 c

4.1.1. Brief partial review of observations

Wagner et al. (2018) reported the detection using MagAO of an $H\alpha$ signal from PDS 70 b, a companion in the gap in the transitional disc around a young (5.4 ± 1.0 Myr; Müller

et al. 2018) pre-main sequence $0.9\text{--}1.0 M_\odot$ star (Keppler et al. 2019; Wang et al. 2021) discovered by Keppler et al. (2018). Then, the $H\alpha$ detection at PDS 70 b was confirmed by Haffert et al. (2019) using VLT/MUSE (Bacon et al. 2010). They also reported the discovery in $H\alpha$ of PDS 70 c, a companion at the edge of the gap. From new VLT/SINFONI K-band data from Christiaens et al. (2019b), Christiaens et al. (2019a) inferred the presence of a circumplanetary disc around PDS 70 b, the first observational evidence for a disc around a planet in a circumstellar disc. Using the near-infrared (NIR) SED and the models of Eisner (2015), they derived an accretion rate $\dot{M} \sim 10^{-7.5} M_J \text{ yr}^{-1}$. Also, Wang et al. (2020) observed this system with Keck/NIRC2 and estimated the mass accretion rate to be $\dot{M} = (3\text{--}8) \times 10^{-7} M_J \text{ yr}^{-1}$ by comparing to the luminosity-evolution model of Ginzburg & Chiang (2019). More recently, Stolker et al. (2020a) added the first detection of PDS 70 b at $4\text{--}5 \mu\text{m}$ and re-analyzed the other data from 1 to $4 \mu\text{m}$, confirming the finding by Wang et al. (2020) that a blackbody fits well the SED. Given their modeling results, they concluded that PDS 70 b is likely surrounded by some dusty material, which nevertheless lets (some) $H\alpha$ pass through. Finally, thanks to $R \approx 500 K$ -band spectra and astrometry of PDS 70 b and c from VLTI/GRAVITY, Wang et al. (2021) found statistical support for a more complex (non-blackbody) SED and for a small mass for PDS 70 b ($M_p < 10 M_J$, but likely even lighter).

The $H\alpha$ signal of PDS 70 b has been detected with two different instruments, with different luminosity determinations. From Wagner et al. (2018), the luminosity can be derived as $L_{H\alpha} = (1.4 \pm 0.6) \times 10^{-6} L_\odot$ following their data and description (see Appendix D for details); this agrees with $L_{H\alpha} = (1.3 \pm 0.7) \times 10^{-6} L_\odot$ derived by Thanathibodee et al. (2019). As for Haffert et al. (2019), they obtain $L_{H\alpha} = (1.6 \pm 0.1) \times 10^{-7} L_\odot$ for PDS 70 b and $(7.6 \pm 1.3) \times 10^{-8} L_\odot$ for PDS 70 c. Thus the luminosity for PDS 70 b derived under the assumption of no extinction within the system, and ignoring the ISM contribution of $A_R \approx 0.02\text{--}0.12$ mag (see Appendix D), is about lower by one order of magnitude than in Wagner et al. (2018).

Hashimoto et al. (2020) improved the data-correction method of the VLT/MUSE data and estimated higher values $L_{H\alpha} = (3.3 \pm 0.1) \times 10^{-7} L_\odot$ and $(1.3 \pm 0.1) \times 10^{-7} L_\odot$ for PDS 70 b and c, respectively. The value for PDS 70 b is still lower than in Wagner et al. (2018) by a factor of four. This could be due to intrinsic variability in the $H\alpha$ emission from PDS 70 b and/or from the known variability of the star in the R band, combined with the way the contrast is measured. However, Haffert et al. (in prep.) report that for a dozen MUSE measurements over a period of three months, there is no variability in the $H\alpha$ flux at the $\approx 30\%$ level. More recently, Zhou et al. (submitted) detected PDS 70 b at $H\alpha$ with the *Hubble Space Telescope* (HST) and also found

¹⁰ At extremely low $f_{\text{fill}} \lesssim 10^{-4}$, self-absorption becomes very important. For more moderate values $f_{\text{fill}} \gtrsim 10^{-3}$ as inferred for young accreting stars (Ingleby et al. 2013), self-absorption is not a significant effect.

¹¹ A recent addition to this list may be 2M0249 c (Chinchilla et al. 2021), with the caveat that chromospheric activity could be contributing to the $H\alpha$.

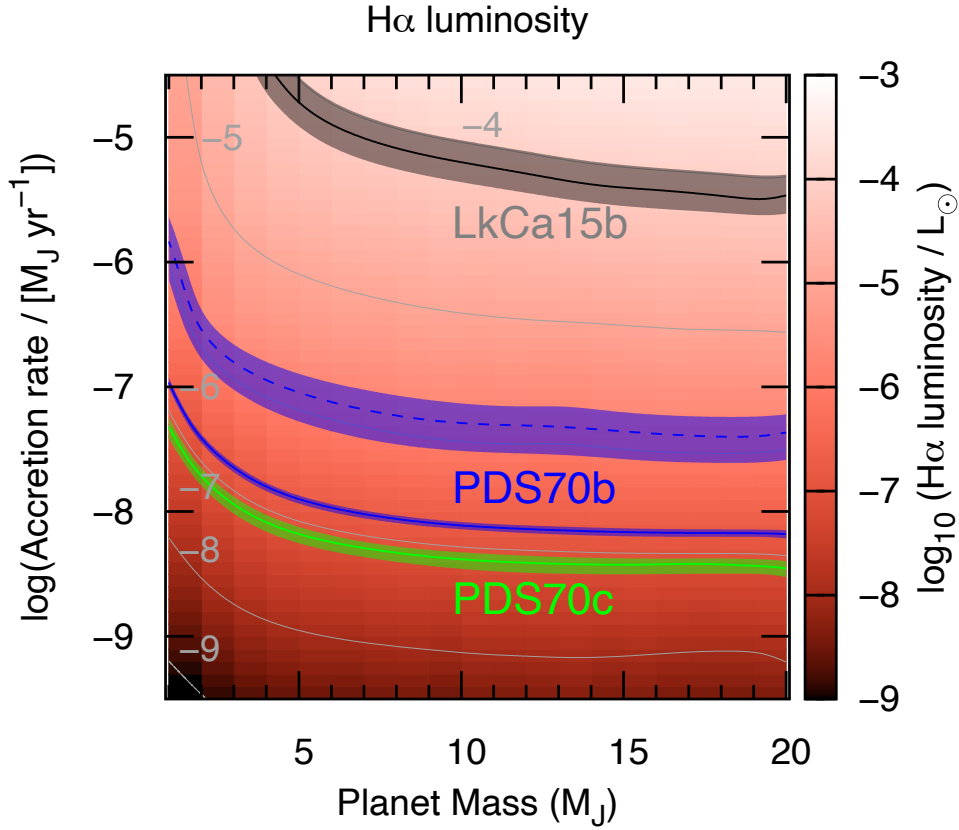


Figure 9. Non-extincted $H\alpha$ luminosity from the planet-surface shock as a function of accretion rate and planet mass (colorscale). Thin gray lines highlight $\log L_{H\alpha}/L_{\odot} = -9$ to -4 in steps of 1 dex. Shaded bands show non-dereddened $1\text{-}\sigma$ contour regions for PDS 70 b (dashed blue line: $10^{-5.9} L_{\odot}$; Wagner et al. 2018; solid: $10^{-6.8} L_{\odot}$; Haffert et al. 2019) and PDS 70 c (green: $10^{-7.1} L_{\odot}$; Haffert et al. 2019). The contour for the Hashimoto et al. (2020) value of $L_{H\alpha} = 10^{-6.5} L_{\odot}$ (not shown) would lie between the two blue bands. The gray region is for the less secure protoplanet candidate LkCa 15 b (black: $10^{-4.1} L_{\odot}$; Sallum et al. 2015, but see text).

no evidence for variability over an almost five-month baseline. Thus differences in the data reduction seem to be a likely explanation for the differences.

4.1.2. No extinction at PDS 70 b and c?

While we assumed no extinction in this paper, Hashimoto et al. (2020) found the $H\alpha$ from PDS 70 b and c to be likely strongly extinguished ($A_{H\alpha} > 2.0$ mag for PDS 70 b) based on the spectral width of the $H\alpha$ line and their upper limit on the $H\beta/H\alpha$ fraction. Repeating their analysis with a more realistic opacity law, Marleau et al. (subm.) derive even stronger constraints ($A_{H\alpha} \gtrsim 4\text{--}8$ mag for PDS 70 b).

However, if the observed spectral width is overestimated due to the instrumental resolution (Thanathibodee et al. 2019), other solutions without extinction are allowed (see Figure 3 in Hashimoto et al. 2020): towards lower n_0 and ν_0 , both the flux ratio $H\beta/H\alpha$ and the line widths are smaller, and there are matching combinations with $A_{H\alpha} = 0$ and smaller f_{fill} . Thus, our assumption can be consistent with the observational results. This solution without (or with weak) extinction is preferred by the mass estimate of PDS 70 b and c (Bae et al.

2019; Stolker et al. 2020a; Wang et al. 2021). To confirm whether the $H\alpha$ from PDS 70 b is strongly extinguished, follow-up observations with a higher spectral resolution are needed.

4.1.3. Derived accretion rate

Given these $H\alpha$ luminosities, our model yields $M_p\text{--}\dot{M}$ relations, shown in Figure 9 as line contours: blue dashed (PDS 70 b; Wagner et al. 2018), blue solid (PDS 70 b; Haffert et al. 2019), and green (PDS 70 c; Haffert et al. 2019), respectively. If $M_p = 5\text{--}9 M_J$ for PDS 70 b as (Wagner et al. 2018) estimated and $M_p = 4\text{--}12 M_J$ for PDS 70 c (Haffert et al. 2019), our model implies $\dot{M} = (8.0 \pm 4.8) \times 10^{-8}$ for PDS 70 b's $L_{H\alpha}$ from Wagner et al. (2018), $\dot{M} = (1.1 \pm 0.3) \times 10^{-8}$ for PDS 70 b's $L_{H\alpha}$ from Haffert et al. (2019), and $\dot{M} = (6.3 \pm 3.1) \times 10^{-9} M_J \text{ yr}^{-1}$ for PDS 70 c's $L_{H\alpha}$ from (Haffert et al. 2019), respectively. If instead $M_p \lesssim 5 M_J$, which is preferred for PDS 70 b (Wang et al. 2021) and c (Bae et al. 2019) the constraints on \dot{M} and M_p are more accurately given in a joint form: $\dot{M}M_p \approx 5 \times 10^{-7} M_J^2 \text{ yr}^{-1}$ for the $L_{H\alpha}$ from Wagner et al. (2018), so that $\dot{M} \approx 1.7 \times 10^{-7} M_J \text{ yr}^{-1}$ for $M_p = 3 M_J$, and, for the $L_{H\alpha}$ from Haffert et al. (2019),

$\dot{M}M_p \approx 6.3 \times 10^{-8} M_J^2 \text{ yr}^{-1}$, implying $\dot{M} \approx 2.1 \times 10^{-8} M_J \text{ yr}^{-1}$ at $M_p = 3 M_J$. Towards low masses, these results depend somewhat more on the choice of the radius fit (see Figure 15), but the main source of uncertainty is the one in the observed value of $L_{H\alpha}$.

By extrapolating the empirical $L_{\text{acc}}-L_{H\alpha}$ relationship for Young Stellar Objects (YSOs) from Rigliaco et al. (2012), Wagner et al. (2018) estimated $\dot{M} \approx 10^{-9} M_J \text{ yr}^{-1}$ for PDS 70 b. Also, with the \dot{M} -linewidth relationship of Natta et al. (2004), Haffert et al. (2019) derived $\dot{M} \approx 2 \times 10^{-8} M_J \text{ yr}^{-1}$. Thus, applying stellar accretion models to planetary-mass observations yields a lower mass accretion rate than from our model by a few orders of magnitude. To estimate mass accretion rates, we suggest that our model constructed for planet accretion should be used rather than the extrapolation of empirical relationship from pre-main-sequence star studies. This is discussed briefly in Section 6.1 but in more details in a companion publication, Aoyama et al. (submitted).

Also, Thanathibodee et al. (2019) constructed a model of $H\alpha$ emission focusing on PDS 70 b. They modeled the *accreting gas* as the source of the $H\alpha$ rather than the postshock region that is the subject of this paper. The accretion rate they estimate, $\dot{M} \approx 10^{-8.0 \pm 0.6} M_J \text{ yr}^{-1}$, is larger than the results of empirical $L_{H\alpha}-L_{\text{acc}}$ relationships and in agreement with our results within the margin of error. As discussed in Section 6.1, whether the $H\alpha$ emission originates from the accretion flow or the postshock region depends on whether the accreting gas is hot enough to emit $H\alpha$. In fact, for PDS 70 b a contribution from both cannot be excluded (Aoyama et al. submitted).

Finally, the upper limits on the Br α (Stolker et al. 2020a) and Br γ (Christiaens et al. 2019b; Wang et al. 2021) emission are discussed in Section 5.4.

In summary, given an $L_{H\alpha}$ measurement, our model yields joint constraints on \dot{M} and M_p at low masses, which seem more likely for PDS 70 b and for PDS 70 c. (For higher masses, $L_{H\alpha}$ becomes relatively independent of M_p .) The uncertainty in \dot{M} is ≈ 1 dex. Our estimated \dot{M} values for PDS 70 b and c are smaller than previously determined in the stellar literature and similar to the results of Thanathibodee et al. (2019). This is however a coincidence, since the two models have a very different physical basis and predict in general distinct $\dot{M}-L_{H\alpha}$ relationships (Aoyama et al. submitted). The main limitations on determining \dot{M} are the uncertainties on the line-integrated fluxes and the line widths, as well as the uncertainties about the true masses.

4.2. LkCa 15 b

Following the discovery of a companion to LkCa 15 A by Kraus & Ireland (2012), Sallum et al. (2015) reported the infrared detection of further sources in the system using sparse-

aperture masking (SAM). Intriguingly, they also measured an $H\alpha$ signal which seemed to originate at the position of LkCa 15 b. On the other hand, Thalmann et al. (2016) analyzed scattered light from the disk and showed that the infrared detections of the planetary candidates around LkCa 15 A could be false positives related to features of the disc in scattered light. In addition, observations by Mendigutía et al. (2018) using spectro-astrometry suggest that the $H\alpha$ emission may not be coming from a point source but rather from an extended region similar in size to the orbit of the claimed planet LkCa 15 b. Recently, Currie et al. (2019) conducted the first direct-imaging observations of the LkCa 15 system. They provided evidence that there is no point source at the location of the claimed planet (nor of the possible further companions) but that in fact the SAM signal originates from disc emission.

Despite the debate as to its origin, we will briefly analyze the $H\alpha$ signal at the position of a putative companion to LkCa 15 A as originating from an accretion shock on the planet surface. The reported $H\alpha$ luminosity is $L_{H\alpha} = 10^{-4.1 \pm 0.1} L_\odot$ from Sallum et al. (2015) but using the updated Gaia distance determination of 158.8 pc (Gaia Collaboration et al. 2018). From Figure 9 and assuming $M_p = 10 M_J$, $\dot{M} = 4.0^{+2.5}_{-0.1} \times 10^{-6} M_J \text{ yr}^{-1}$. This accretion rate is not implausible for a claimed forming gas giant, especially if it were undergoing an accretion outburst.

Using instead the Rigliaco et al. (2012) approach as in Sallum et al. (2015) and again with $M_p = 10 M_J$ as an example, yields $\dot{M} = 3 \times 10^{-7} M_J \text{ yr}^{-1}$ for $R_p = 1.6 R_J$ as Sallum et al. (2015) assumed. At this (\dot{M}, M_p) , our fits (Section 2.1.1) yield $R_p = 1.9 R_J$ ($R_p = 1.4 R_J$) for the hot (cold) population, so that 1.6 R_J is a reasonable value, albeit perhaps on the small side. The upshot of the comparison is that the \dot{M} implied by the Rigliaco et al. (2012) relationship is one order of magnitude smaller than derived with our approach; for PDS 70 b, it was a few orders of magnitude. As discussed in Aoyama et al. (submitted), we suggest that our models, which are tailored for the planetary case, should be used instead of extrapolations from the stellar regime.

5. FURTHER OBSERVATIONAL ASPECTS

We now discuss to what extent high-mass and high- \dot{M} planets can be distinguished (Section 5.1) and the planet surface shock from the CPD shock (Section 5.2), before presenting the line strengths and line ratios for accretion-generated hydrogen lines other than $H\alpha$ (Section 5.3). Finally, we discuss what information may be obtained from combining observations of several lines for the same object (Section 5.4).

5.1. Distinguishing massive planets and strongly accreting planets from the line profile?

When characterizing gas giants from their $H\alpha$ luminosity, their mass and mass accretion rate are degenerate because the

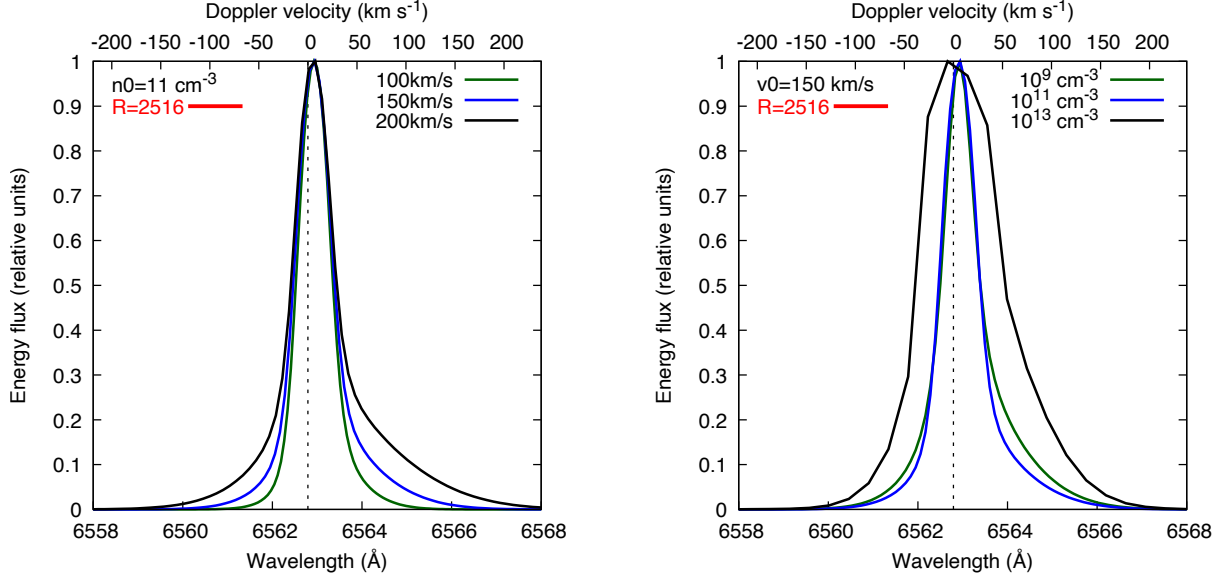


Figure 10. Spectral profile of $H\alpha$ for $v_0 = 100, 150, 200 \text{ km s}^{-1}$ at $n_0 = 10^{11} \text{ cm}^{-3}$ (left panel) and for $n_0 = 10^9, 10^{11}, 10^{13} \text{ cm}^{-3}$ at $v_0 = 150 \text{ km s}^{-1}$ (right panel), typical for planetary masses (see Figure 4). Each line is normalized by its peak value. The top axis shows the Doppler shift velocity, even though some features come from natural and not Doppler broadening. The spectral resolution of MUSE at $H\alpha$ is indicated ($R = 2516$; red bar). The $H\alpha$ line width depends on n_0 more than on v_0 because high n_0 leads to self-absorption near the peak.

luminosity depends on their product. However, this degeneracy can be lifted by spectroscopic observations of $H\alpha$, which was demonstrated by Aoyama & Ikoma (2019) in the case of PDS 70 b and c.

Recall that the preshock velocity v_0 mainly depends on M_p , while the number density n_0 is mainly set by \dot{M} (see Figure 5). Figure 10 shows $H\alpha$ line shapes for several values of v_0 and n_0 . The preshock velocity v_0 sets the shock strength—and thus the temperature just after the shock (Equation (17))—but barely the line width, which is mainly set by Doppler broadening. This is because the gas that becomes ionized and then recombines is the main source of $H\alpha$, and not the gas immediately after shock, even if there is some amount of excited hydrogen there (see down to $\Delta t \approx 10^{-3} \text{ s}$ in Figure 6). Note that Figure 10a a small redshift (of several km s^{-1}) can be seen in the line profiles. This is due to the non-zero settling speed of the emitting gas.

The line profile can be divided into three parts: a narrower Gaussian, a broader Gaussian, and a Lorentzian profiles, with the latter visible further from the line center. The layers that emit the two Doppler profiles are separated by the highly ionized region (at $\Delta t \approx 10^{-3}$ – 10 s in Figure 6). The $H\alpha$ intensity coming from the deeper layers is much larger. Consequently, even the width of the line where the energy density is 10% of the maximum (W_{10} in e.g. Thanathibodee et al. 2019) reflects only the narrower Doppler component, coming from the hydrogen-ion recombination region at low temperatures, in the deep layers. The gas temperature at which hydrogen recombination begins barely depends on v_0 , because it corresponds to the hydrogen ionization energy of 13.6 eV. We can

see the thermal broadening of the optically thinner gas just after the shock only far from the line center, at $\lambda \gtrsim 6564 \text{ \AA}$ and $\lesssim 6562 \text{ \AA}$ (i.e., $|\Delta v| \gtrsim 50 \text{ km s}^{-1}$ away from the shock). Since the hot gas immediately below the shock has a high velocity and is travelling away from the observer, the red half of the line is more broadened by this mechanism than the blue half. However, as seen in the right panel, the resolution of MUSE ($R = 2516$ at $H\alpha$; Eriksson et al. 2020) is not sufficient to distinguish this.

As shown in the right panel of Figure 10, n_0 changes the width of the *normalized* line dramatically. However, increasing n_0 hardly broadens the $H\alpha$ line because the pressure broadening is negligible relative to the natural broadening. A high n_0 leads to $H\alpha$ self-absorption in the postshock gas (in the top part of the flow), which flattens the line peak. Since we normalized the line flux at the peak, the self-absorbed line looks broader (see Aoyama et al. 2018 for the non-normalized profile). However, the lines for higher n_0 are brighter than lower ones despite the absorption. This effect becomes significant for $n_0 > 10^{11} \text{ cm}^{-3}$ in the right panel. Also, a lower n_0 (10^9 cm^{-3}) can lead to slightly broader profile. While the wider component that comes from the shallower region is independent of the density, the narrower component that comes from the deeper region gets weaker with decreasing n_0 due to a lower excitation degree. Thus, the wider component gets stronger relative to the narrower component.

As shown in Figure 10, the current spectral resolution of MUSE is not enough to distinguish the profiles clearly, while it barely resolves the spectral profile for higher density (Eriksson et al. 2020). However, it is not possible to determine in

general what minimum spectral resolution is required for distinguishing high accretion rates from high masses because it depends on the relative uncertainty in the flux as well as on the planet properties through the dependence of the line profile on (n_0, v_0) .

5.2. Distinguishing planetary-surface and CPD-surface shocks?

Hydrodynamic simulations report that gas accreting toward proto-gas-giants goes through multiple shocks (e.g. Kley 1999; Tanigawa et al. 2012). The gas that falls onto the CPD yields a shock, which can emit $H\alpha$ near the planet. However, far from the planet, the shock is not strong enough to emit $H\alpha$, and only the part of the shock close to the planet can contribute to the $H\alpha$ emission (Aoyama et al. 2018). If the gas ultimately joining the planet passes firstly through a shock at the surface of the CPD and secondly through the planetary surface shock, the former is negligible for $H\alpha$ emission, because most of the gas hits the CPD at the far region. There, the free-fall velocity is too small for significant $H\alpha$ emission. For example, when the CPD is truncated near the planet (and the gas is accreting by magnetospheric accretion or it is falling directly onto the planet from the PPD), the planetary surface shock dominates the emission. However, when most gas passes through boundary-layer accretion (see, e.g., Dong et al. 2020 rather than a planetary surface shock, the CPD surface shock becomes significant. Thus it would be desirable to distinguish the source of shock excess.

In Figure 11, we compare the SEDs from the planetary surface shock and the CPD surface shock. The shock excess from the latter highly depends on the gas accretion model. Here, guided by the results of an isothermal 3D hydrodynamic simulation (Tanigawa et al. 2012), we assume the following:

1. All gas accretes vertically from the protoplanetary disk onto the CPD with a free-fall velocity starting from infinity set by the protoplanet's gravity, $v_{\text{ff}}(r) = \sqrt{2GM_p/r}$, where r is the radial distance from the protoplanet's center.
2. The mass accretion flux onto the CPD is spatially constant within 0.1 Hill radius, and zero outside of this. The inner disc radius does not matter because the contribution of the outer region to the intensity dominates over that of the inner region (Aoyama et al. 2018).

Non-isothermal simulations might find a different flow pattern (especially concerning assumption 2.) but this should capture qualitatively the main differences between the planet-surface and CPD-surface shock cases.

As an example, we consider system parameters that could be appropriate for PDS 70 b. The semi-major axis is 22.6 au and the central-star mass is $0.82 M_\odot$ (Riaud et al. 2006). The mass of PDS 70 b is very uncertain, with some indications for

a low mass of a few M_J (Mesa et al. 2019; Stolker et al. 2020a). Here, we choose a somewhat high value within the range considered in the literature, namely $M_p = 8 M_J$ (Wagner et al. 2018). This places us in the flat part of the $L_{H\alpha}(\dot{M}, M_p)$ contours, making the choice of \dot{M} simple for the surface-shock case, with $\dot{M} = 10^{-7} M_J \text{ yr}^{-1}$. To have the same $H\alpha$ luminosity $L_{H\alpha} \approx 1.5 \times 10^{-6} L_\odot$ in the CPD-shock case (Wagner et al. 2018), we take for the CPD-shock case $\dot{M} = 10^{-3} M_J \text{ yr}^{-1}$, with the same mass. In both cases, we set $R_p = 1.7 R_J$ and $T_{\text{eff}} = 1600 \text{ K}$ (Section 2.1). For the surface-shock case, $f_{\text{fill}} = 1$ is also assumed.

What fraction of the accreting gas in the CPD-shock case can produce hydrogen lines? The chosen parameters yield $R_{\text{Hill}} \approx 7000 R_J = 3.3 \text{ au}$. From Figure 4, at this mass only the gas within $r \approx 30 R_J$ has $v_{\text{ff}} \gtrsim 30 \text{ km s}^{-1}$ and thus contributes to $H\alpha$. This region corresponds to $0.005 R_{\text{Hill}}$, and thus 0.2 % of the area over which the gas is assumed to accrete. Thus only this small fraction of the accretion rate is available for producing $H\alpha$. This partly explains the need for a high total \dot{M} compared to the surface-shock case to have the same $L_{H\alpha}$. The other reason is that v_0 is smaller everywhere on the CPD than on the planet surface (see Figure 4), so that \dot{M} must be higher to compensate since $F_{H\alpha}$, the $H\alpha$ flux at the object's surface, roughly scales with the incoming kinetic energy flux $F_{\text{acc}} \propto n_0 v_0^3$.

The left panel of Figure 11 displays the global SEDs. The red and blue lines correspond to the SED assuming planetary surface shock and CPD surface shock, respectively. The black line corresponds to the SED without a shock excess for reference. In the Lyman and Balmer continua, namely for $\lambda \lesssim 3000 \text{ \AA}$, the two SEDs differ by more than a factor of ten. This comes from the difference in gas temperature after the two shocks. For the CPD surface shock, the regions far from the planet dominate the shock excess emission because of their large emitting area. This is a relatively weak shock, associated with a low temperature.

This temperature difference can be also seen in the $H\alpha$ profile in Figure 11b: the profile is narrower in the CPD surface-shock case than in the planet surface-shock case when taking the different heights into account (i.e., looking at the full width at half-maximum (FWHM)). The difference is small but might be detectable in the future with high-resolution observations. For example, for the case of Figure 11, the wavelength difference at the 10% of the peak corresponds to 17 km s^{-1} , which is distinguishable with the spectral resolution of $R \approx 18,000$ (which is much higher than the resolution of MUSE with $R \approx 2500$). At lower flux levels relative to the peak, the difference is greater (e.g., $\approx 25 \text{ km s}^{-1}$ at 5%) but it is not clear whether such levels can be robustly extracted because of the high contrast relative to the peak. The continuum emission from the CPD (Zhu 2015) or from the planet's photosphere are likely not important, but the star's

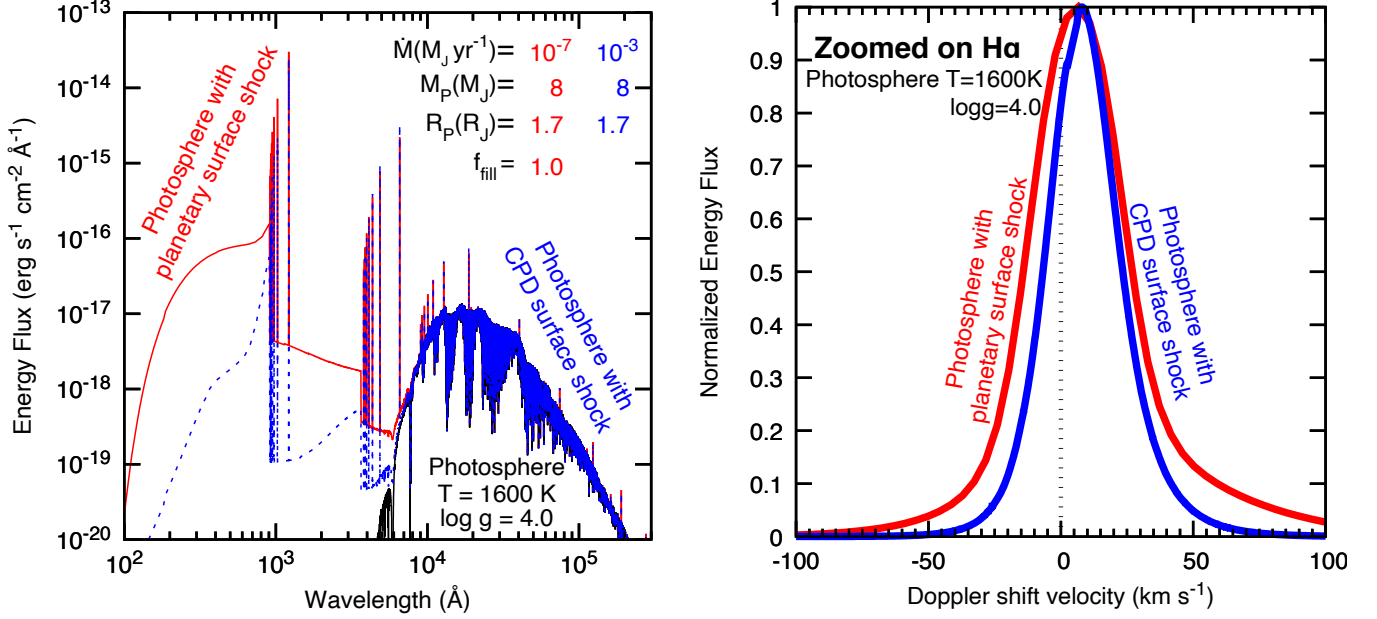


Figure 11. SEDs for two different models of shock-heated gas emission: planetary photospheric emission plus planetary-surface shock (red) and CPD surface-shock (blue). The photosphere SED in the surface-shock case is also shown for reference (black). The \dot{M} , M_p , R_p values (see figure and text) are chosen such that $L_{H\alpha} \approx 1.5 \times 10^{-6} L_\odot$ in both cases. The energy flux is calculated for the distance of 150 pc. *Left panel:* Global SED. *Right panel:* $H\alpha$ line profile against Doppler shift velocity from the line center. The photospheric emission is not visible.

chromosphere could contribute (Manara et al. 2013, 2017; Venuti et al. 2019). The stellar accretion-induced $H\alpha$ is possibly Doppler-shifted away from the planet’s signal as in Haffert et al. (2019). However, the most important limitation is probably the maximal contrast allowed by the instrument.

The narrower $H\alpha$ and the weaker recombination continua in the CPD case means a weaker shock, which can also occur at the surface of a less massive planet. However, in such a case, the density should be higher than the CPD case, and one can distinguish these two cases.

Our model does not include some continuum sources such as a heated photosphere (e.g. Königl 1991; Calvet & Gullbring 1998) or, if present, the boundary layer (e.g. Kenyon & Hartmann 1987; Dong et al. 2020), which are well modeled in the stellar accretion context. Such continuum sources can change the spectral appearance, but it is unfortunately difficult to say how important this would be.

In summary, for a given $H\alpha$ luminosity, the resolution of MUSE is not sufficient to distinguish an accretion shock on the planetary surface from the one on the CPD, but high-resolution spectroscopy might be able to do so.

5.3. Predictions for hydrogen lines other than $H\alpha$

The $H\alpha$ line on which we have focused so far is only one of the 55 hydrogen lines we model. Recently, Eriksson et al. (2020) reported an $H\beta$ flux for the ≈ 10 - M_J companion Delorme 1 (AB)b with the MUSE instrument on the VLT.

Also, the upcoming, first-light HARMONI¹² integral field unit (IFU; Thatte et al. 2016; Rodrigues et al. 2018) on the ELT is expected to provide $R \approx 17,000$ spectroscopy between 0.8 and 2 μm (thus including for instance $\text{Pa}\beta$ and $\text{Br}\gamma$); the second-generation instrument HIRES for the ELT (Marconi et al. 2016, 2018; Tozzi et al. 2018) will cover 1–1.8 μm and thus should observe Paschen lines with the high spectral resolution of $R \approx 100,000$; and the University of Tokyo Atacama Observatory (TAO) should be able to detect $\text{Pa}\alpha$ thanks to its location at 5,640 m (Yoshii et al. 2010). Finally, the Keck Planet Imager and Characterizer (KPIC) (Jovanovic et al. 2019; Morris et al. 2020) aims at obtaining $R = 35,000$ spectroscopy in the K , L , and M bands (≈ 2 –5 μm). Clearly, it is timely to extend the luminosity predictions to lines other than $H\alpha$.

In Figure 12, we show the line luminosity of $H\beta$, $\text{Pa}\alpha$, $\text{Pa}\beta$, and $\text{Br}\gamma$ for the same grid of (\dot{M}, M_p) as in Figure 9. The luminosities range from $L_{\text{line}} \sim 10^{-12}$ to $10^{-4} L_\odot$, increasing with \dot{M} and M_p as for $H\alpha$, and with the same qualitative shape of a very weak mass dependence for $M_p \gtrsim 3$ –5 M_J . The contours are very similar using the fit to the hot- or cold-start populations. We show upper limits for a few objects but discuss them below in Section 5.4.

¹² See <https://harmoni-elt.physics.ox.ac.uk>.

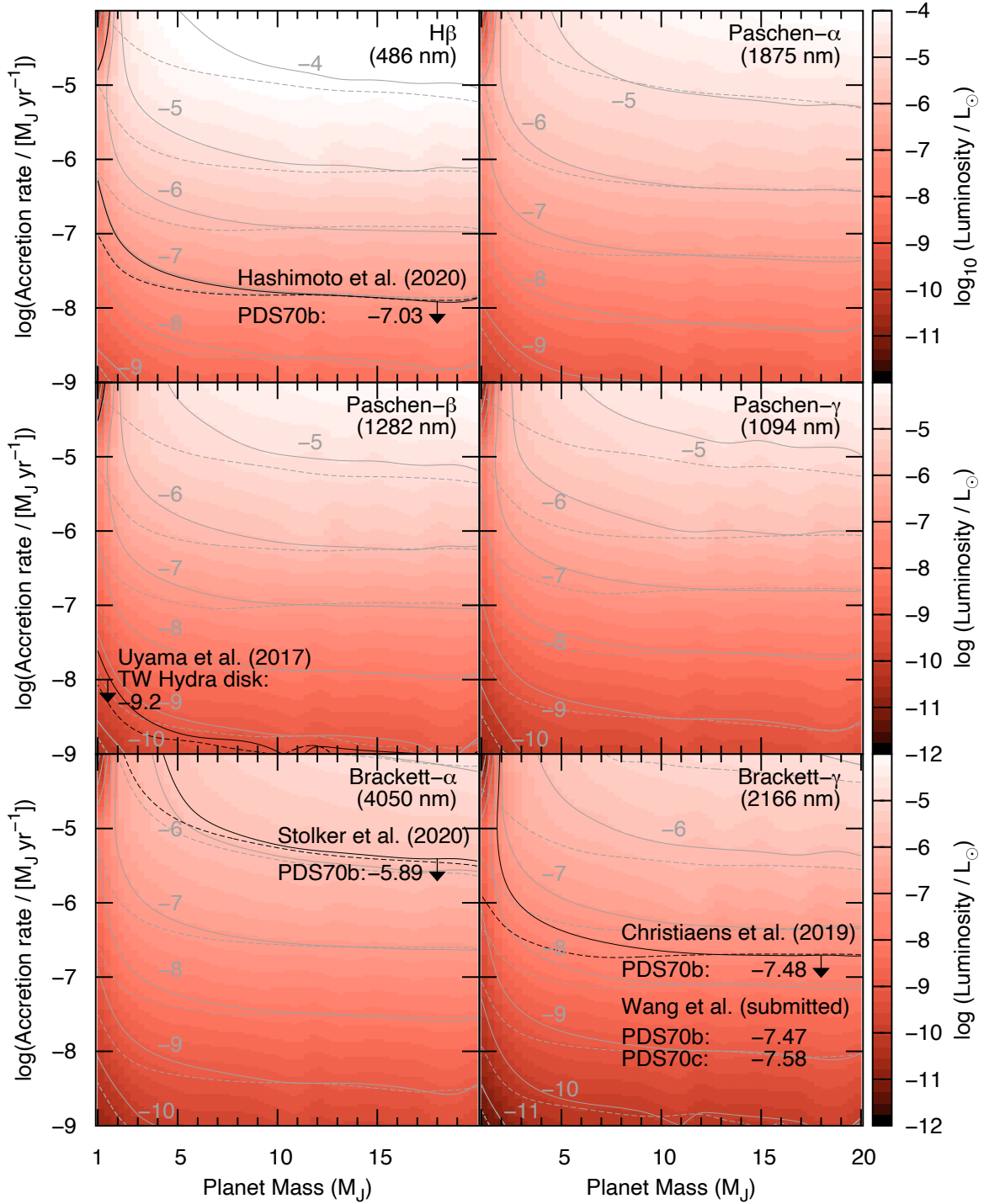


Figure 12. As in Figure 9 but for H β , Pa α , Pa β , Pa γ , Br α , and Br γ . The color map and the solid contour lines show the results from the radius fit to the warm population, and the dashed contour lines use the cold population. Black lines show 5- σ upper limits of $\log(L_{\text{H}\beta}/L_{\odot}) < -7.03$ (Hashimoto et al. 2020) and $\log(L_{\text{Br}\gamma}/L_{\odot}) < -7.48$ (Christiaens et al. 2019b) for PDS 70 b, and of $\log(L_{\text{Pa}\beta}/L_{\odot}) < -9.20$ for a putative planet at 25 au in TW Hya (Uyama et al. 2017). Wang et al. (2021) set Br γ upper limits for PDS 70 b and c similar to the line of Christiaens et al. (2019b). In the Br α panel, black contours are for the detected flux at NACO/NB4.05, $\log(L_{\text{Br}\alpha}/L_{\odot}) = -5.88$ (Stolker et al. 2020a), which is an upper limit on the line flux if the continuum is much stronger, as is expected.

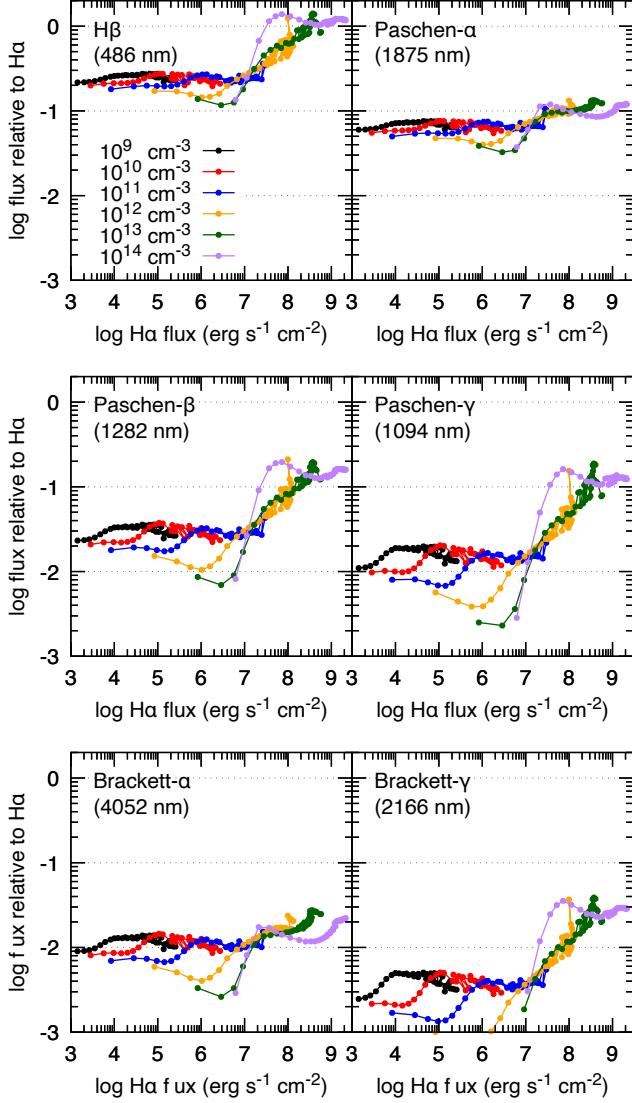


Figure 13. Flux of $H\beta$, $Pa\alpha$, $Pa\beta$, $Pa\gamma$, $Br\alpha$ and $Br\gamma$ relative to $H\alpha$ as a function of the $H\alpha$ flux at the surface of the object $F_{H\alpha}$ and the preshock number density $n_0 = 10^9$ – 10^{14} cm^{-3} (colour). For each n_0 , the preshock velocity v_0 is varied from 20 to 200 km s^{-1} . The $H\alpha$ luminosity is related to the x -axis by $L_{H\alpha} = 4 \times 10^{-8} F_{H\alpha} (R_p/1.5 R_J)^2 (f_{\text{fill}}/1) L_\odot$. The apparent flux $\mathfrak{F}_{H\alpha}$ of an 1.5 - R_J object at 100 pc is given by $\log \mathfrak{F}_{H\alpha} = \log F_{H\alpha} - 20.9$ dex.

Next, Figure 13 shows the intensity ratio of $H\beta$, $Pa\alpha$, $Pa\beta$, and $Br\gamma$ relative to $H\alpha$ as a function of the $H\alpha$ flux at the surface of the object. (Absolute fluxes for $H\beta$, $Pa\alpha$, and $Pa\beta$ as a function of (n_0, v_0) can be found in Aoyama et al. (2018).) The ratios span $H\beta/H\alpha \approx 0.1$ – 2 to $Br\gamma/H\alpha \approx 0.001$ – 0.05 , with typically $X/H\alpha \approx 0.03$ – 0.3 for $X = H\beta, Pa\alpha, Pa\beta$.

All four ratios are more or less flat within 0.5 dex at low $H\alpha$ flux (within 0.7 dex for $Br\gamma/H\alpha$) but start to increase around an $H\alpha$ flux $F_{H\alpha} \sim 10^7$ $\text{erg s}^{-1} \text{cm}^{-2}$. For $Pa\alpha$ the rise is only moderate. This change of slope occurs because

the $H\alpha$ saturates due to self-absorption in the shock-heated gas as v_0 increases, while the other lines do not saturate. Thus towards high $F_{H\alpha}$, v_0 must increase faster along the x axis, which leads to stronger other lines (and thus ratios) since they hardly display self-absorption. Also, when the starting level of the transition is high (i.e., $Pa\beta$ or $Br\gamma$: $n = 5 \rightarrow 3$ or $n = 7 \rightarrow 4$, respectively), some features at weaker $H\alpha$ ($F_{H\alpha} \lesssim 10^6$ $\text{erg s}^{-1} \text{cm}^{-2}$) become more clearly visible. To understand this, one should recall that for a given n_0 , a low $H\alpha$ flux means a low gas temperature, and that for low temperatures, $F_{H\alpha}$ increases faster than the other lines due to its lower excitation energy, and conversely at higher temperatures. Therefore, the ratio first decreases and then increases towards high temperature ($F_{H\alpha}$).

Also, our model predicts that the $Ly\alpha$ is much stronger than all lines and carries most of the incoming shock energy, which has been converted to radiation (see Figures 6 and 8). This is an important input for models of CPD chemistry (Cleeves et al. 2015; Rab et al. 2019). However, interstellar extinction is too strong for $Ly\alpha$ to be detected, excepting a few young stellar systems such as TW Hydra. However, other lines induced by planetary $Ly\alpha$ might be detected as for some accreting stars, including NIR fluorescent molecular hydrogen lines (e.g., Herczeg et al. 2004).

Finally, Zhou et al. (submitted) detected for the first time PDS 70 b in the Balmer continuum with the F336W (U -band) filter of HST. While our model does predict hydrogen recombination continua, it is constructed with a focus on the hydrogen lines. The predicted continua are less reliable and likely overestimated especially for the massive planets. This is because where the gas is almost ionized, the only effective coolant in our model are the recombination continua, while metal lines (for instance O I; Hollenbach & McKee 1989) should play an important role. This would decrease the fluxes currently predicted in the continua. To treat them more accurately, a model update is planned in the future.

5.4. Combining detections of multiple accretion lines

We briefly discuss the few current application of these predictions in the planetary-mass regime. Firstly, the $5\text{-}\sigma$ $Br\gamma$ upper limit for PDS 70 b from Christiaens et al. (2019b), $\log L_{Br\gamma}/L_\odot < -7.48$, is shown in Figure 12. From $R \approx 500$ VLT observations, Wang et al. (2021) confirmed this upper limit to within 0.01 dex, and also placed a similar $5\text{-}\sigma$ limit of $\log L_{Br\gamma}/L_\odot < -7.58$ for PDS 70 c. Taken at face value, this implies for PDS 70 b that $\dot{M} \leq 2 \times 10^{-7} M_J \text{yr}^{-1}$ (and somewhat less for PDS 70 c) if $M_p \gtrsim 8 M_J$, but is much less constraining at lower M_p .

Also, Stolker et al. (2020a) detected PDS 70 b for the first time in the $Br\alpha$ filter of NACO/VLT (NB4.05; the effective

width is $0.0616 \mu\text{m}$ and not $0.02 \mu\text{m}^{13}$). The $\text{Br } \alpha$ line can be used as an accretion tracer (Komarova & Fischer 2020), but in this case the flux is consistent with the blackbody emission matching the global SED. Namely, given the observed $\text{H } \alpha$ flux, the $\text{Br } \alpha$ is expected to be embedded in the continuum (see Figure 13), and the upper limit of the $\text{Br } \alpha$ emission from the shock itself is the observed line-integrated luminosity of $L = 1.3 \times 10^{-6} L_{\odot}$. This implies that $\dot{M} \leq 10^{-5} M_{\text{J}} \text{ yr}^{-1}$ if $M_{\text{p}} \gtrsim 5 M_{\text{J}}$, which is a mass range not favoured by the analysis of Wang et al. (2021) but not completely unlikely. For M_{p} of at most a few M_{J} , which seems more plausible (Stolker et al. 2020a; Wang et al. 2021), the $L_{\text{Br } \alpha}$ upper limit is effectively not constraining, with $\dot{M} \leq 10^{-4} M_{\text{J}} \text{ yr}^{-1}$. Such high rates are barely expected from the theoretical side. Even the somewhat lower upper limits at high masses are consistent with the results from Figure 9, $\dot{M} \approx 8 \times 10^{-8} M_{\text{J}} \text{ yr}^{-1}$ from the Wagner et al. (2018) measurement or $\dot{M} \approx 1 \times 10^{-8} M_{\text{J}} \text{ yr}^{-1}$ from Haffert et al. (2019).

For comparison, Hashimoto et al. (2020) derived from their re-analysis of archival MUSE data an $\text{H } \beta$ flux upper limit of $2.3 \times 10^{-16} \text{ erg s}^{-1} \text{ cm}^{-2}$ for PDS 70 b, corresponding to $L_{\text{H } \beta} < 9.2 \times 10^{-8} L_{\odot}$ (3σ). This $\text{H } \beta$ is inconsistent with the $\text{H } \alpha$ result (see Figure 9). The same is true for PDS 70 c. From this, Hashimoto et al. (2020) concluded that there must be differential extinction. As justified in Section 2.3, we emphasise that our results are *without* taking extinction into account, which we do separately in Marleau et al. (subm.).

In the same class as CT Cha B/b or DH Tau B/b, some of the only low-mass putative accretors for which other accretion lines have been detected (Schmidt et al. 2008; Bonnefoy et al. 2014; Zhou et al. 2014; Bowler et al. 2014; Wu et al. 2015), is Delorme 1 (AB)b, for which Eriksson et al. (2020) measured $\text{H } \beta$ (and also He I lines and upper limits on the infrared Ca II triplet). They infer a mass $M_{\text{p}} \approx 12 M_{\text{J}}$ and radius $R_{\text{p}} = 1.6 R_{\text{J}}$ from (hot-start) evolutionary models by combining their results to the photometry of Delorme et al. (2013). They report $\log(L_{\text{H } \alpha}/L_{\odot}) = -7.05 \pm 0.06$, from which they infer $\dot{M} \approx (0.8\text{--}3.0) \times 10^{-8} M_{\text{J}} \text{ yr}^{-1}$ by combining their $L_{\text{H } \alpha}$ measurement with different models. Combined with ours (Aoyama et al. 2018; Aoyama & Ikoma 2019; this work), they derive $\dot{M} = 1 \times 10^{-8} M_{\text{J}} \text{ yr}^{-1}$ and $M_{\text{p}} = 11 M_{\text{J}}$, using the radius $R_{\text{p}} = 1.6 R_{\text{J}}$ suggested by the photometry. From Figure 12, the predicted $\text{H } \beta$ luminosity is $L_{\text{H } \beta} \approx 4 \times 10^{-8} L_{\odot}$. However, Eriksson et al. (2020) measured $L_{\text{H } \beta} = 10^{-8} L_{\odot}$, which is a factor four lower than the model prediction. This suggests

that as for PDS 70 b, extinction is affecting the measurement of accretion tracers. The interesting difference is that there is up to now no evidence for an accretion disc around Delorme 1 (AB)b, but the constraints on a disc mass or surface density are not clear (Eriksson et al. 2020). Thus a detection of (or upper limit on) a disc around Delorme 1 (AB)b, as well as more observational information on other hydrogen lines would be useful. On the theoretical side, predictions for the other currently available lines (He I and the infrared Ca II triplet) would be welcome.

Finally, in Figure 12, we show the $5\text{-}\sigma$ upper limit on $\text{Pa } \beta$ emission for the TW Hya disc in its gap at 25 au, $\log(L_{\text{Pa } \beta}/L_{\odot}) < -9.20$, derived by Uyama et al. (2017) using Keck. At 95 au, where there is an other gap, the upper limit is $\log(L_{\text{Pa } \beta}/L_{\odot}) < -9.79$ (not shown). This is consistent with the mass constraints of $M_{\text{p}} \lesssim 0.5 M_{\text{J}}$ from van Boekel et al. (2017) for TW Hya. Looking at Figure 12, the interesting implication is that Keck at $\text{Pa } \beta$ is sensitive to planets with a relatively low mass or accretion rate, at least for the nearest protoplanetary discs.

6. DISCUSSION

We now take a critical look at different aspects of the model and results presented in this work (Sections 6.1–6.4), and discuss the non-detections of recent $\text{H } \alpha$ surveys (Section 6.5). Some caveats about the model were already discussed in Section 4.2 of Aoyama et al. (2018) and we do not repeat them here. We compare with other recent models of $\text{H } \alpha$ emission from accreting planets (Thanathibodee et al. 2019; Szulágyi & Ercolano 2020) and discuss the validity of their approach in a different work (Aoyama et al. submitted). Appendix A already details why the physical assumptions behind Storey & Hummer (1995) do not apply to the planetary surface shock.

6.1. Emission by the gas accreting onto the planet

Our model treats only the shock-heated gas. Several previous studies focusing on stellar-mass objects considered the gas flowing onto the accretor as the source of observed $\text{H } \alpha$ excess, assuming an unknown source of heating there (e.g. Hartmann et al. 1994; Edwards et al. 2013), as opposed to heating provided by the shock. Since the shock on accreting stars makes the gas too hot ($> 10^6 \text{ K}$) to emit hydrogen lines, the shock-heated gas is negligible for hydrogen-line emission. On the other hand, the planet-surface shock emits significant hydrogen lines, while the accreting gas should be cooler and emit weaker or no hydrogen lines compared to the stellar cases (see also the discussion in Aoyama et al. submitted). This is the reason why we neglect hydrogen line emission from the region.

Even if the gas in the accretion flow is too cool to emit $\text{H } \alpha$, the warm gas plays a significant role in excess emission other than from hydrogen lines. In the T Tauri-star context,

¹³ The too-narrow width came from <http://www.eso.org/sci/facilities/paranal/decommissioned/naco/inst/filters.html> (corrected in January 2021), which however provides the correct filter curve, and is often quoted in the literature (e.g. Janson et al. 2008; Quanz et al. 2010; Meshkat et al. 2014; Kervella et al. 2014; Stolker et al. 2020b,a). It however does not change the results in those studies. The correct value is from the SVO at <http://svo2.cab.inta-csic.es/theory/fps3/index.php?id=Paranal/NACO.NB405>.

Calvet & Gullbring (1998) found that a Balmer recombination continuum is emitted by the gas accreting onto the object rather than the postshock gas. The hydrogen recombination continua are well modeled and compared with observational results in the stellar accretion context. As seen in Figures 7 and 8, the planetary continua are predicted to be several (up to tens of) orders of magnitude stronger than the contribution from the planetary photosphere. Therefore, detecting in the planetary context a hydrogen continuum much stronger than the photospheric emission would lend support to our emission models.

6.2. Effect of the accretion geometry: spherical versus magnetospheric

The predicted $H\alpha$ luminosity (see Figure 9) was derived explicitly in the context of spherical accretion onto the protoplanet's surface. However, it also represents the signal expected for any accreting planet, regardless of the accretion geometry, i.e., spherical or magnetospheric. In the case of magnetospheric accretion with a filling factor $f_{\text{fill}} < 1$, relative to spherical accretion, the kinetic-energy flux locally is higher by $1/f_{\text{fill}}$ but the accreting area is smaller by f_{fill} . These effects cancel each other out to a large extent over most of parameter space. However, more precisely, spherical accretion yields an upper limit to the $H\alpha$ intensity because of $H\alpha$ self-absorption in the shock-heated gas. To emit more intense $H\alpha$ by avoiding self-absorption, the gas needs to be less dense, which, at a given \dot{M} , will be the case for higher f_{fill} . Note that in a realistic situation, the infalling gas and dust could absorb a part of the flux emitted at the planet surface. This is explored systematically in Marleau et al. (subm.).

Also, in the scenario of accretion onto a circumplanetary disk, the $H\alpha$ emission is at most roughly 1% of the $H\alpha$ coming from the planet surface for a similar planet mass, at least for the (simple) disc model and scaling assumed in Aoyama et al. (2018). (In Section 5.2 we had compared the line shapes at fixed total luminosity.) Therefore, when a strong shock occurs on the planetary surface, regardless of the geometry, the CPD surface shock is negligible.

6.3. Helium and metal lines

For accreting stars, helium and metal lines (He I, Ca II, Na I, O I, etc.) are also detected and used as indicators of stellar accretion as for hydrogen lines (e.g. Kastner et al. 2002). At the upper edge of the planetary-mass range, $M_p \approx 20 M_J$ leads to $v_{\text{ff}} \approx 200$ km/s for $R_p = 2R_J$ (see Figure 5), so that the postshock gas temperature can exceed $T_1 \approx 10^6$ K (Equation (17)). In that case, metal lines instead of hydrogen lines are responsible for the dominant emission processes at ultraviolet (UV) wavelengths.

Our estimate of the hydrogen recombination continua would change when including metal lines. When hydrogen ionization proceeds and neutral hydrogen is minor (e.g.

at $T \approx 10^5$ K in Figure 6), the gas should cool through hydrogen recombination continua and/or metal lines. Presently, because we do not include metal lines, almost all the thermal energy is converted into the continua, so that they are overestimated. The hydrogen recombination continua are mostly used as accretion indicator of protostars (e.g. Calvet & Gullbring 1998). For planetary accretion, they are currently expected to highly exceed photospheric emission at UV wavelengths, as in the example in Figure 7, but this should be re-assessed once more complete models are available.

6.4. On the physical size of the cooling region

Towards high v_0 , the line-forming region can be at a depth of order of the planet size, which is clearly unrealistic. By contrast, in Figure 6 it is at $\Delta z \approx 3 \times 10^7$ cm, which represents $0.002R_p$ and is much smaller than the planet size and thus reasonable. The reason for the large extent of the cooling zone in some of the other cases is that (i) there is no cooling by helium nor atomic metals (as opposed to CO, H₂O, and OH, which are included) and (ii) the geometry is assumed to be plane parallel. The latter approximation is an issue only because of the first; if we included cooling by helium and metals, curvature effects would be unimportant as the cooling region would be thin. Nevertheless, currently, the neglect of gravity is a good approximation because the increasing density compensates for the longer cooling timescale by decreasing back the thermal collision timescale. In any case, we remind that we always resolve the line-forming region because of adaptive time-stepping, which keeps the relative change in temperature within 10% per step.

Despite the unrealistically large extent of the cooling region in some cases, the hydrogen-line fluxes should be relatively accurate within the other model assumptions. This is because the hydrogen-line emission occurs in a spatially thin region (as in the example in Figure 6). Where exactly this region is located (i.e., possibly at too large a depth) is inconsequential for its emission properties. Also, towards high n_0 and v_0 , absorption in upper layers of the flow becomes important. Here, the distance between the emission and absorption regions does not matter because the intervening region is optically thin. Including metal-line calculations will lead to thinner cooling regions only as a side effect but the aim will be to obtain the fluxes in the lines themselves. The presence of the heated photosphere (as in Calvet & Gullbring 1998) is more likely to affect the thermal structure of the postshock region as well as the continuum emission but exploring this is beyond the scope of this work.

6.5. Explaining the non-detections

Recent searches (Cugno et al. 2019; Zurlo et al. 2020; Xie et al. 2020) for accreting planets in $H\alpha$ have returned non-detections, with $5\text{-}\sigma$ sensitivities down to line-integrated luminosities $L_{H\alpha} \sim 10^{-7}\text{--}10^{-6} L_\odot$ beyond ~ 15 au

(≥ 100 mas). Using the [Rigliaco et al. \(2012\)](#) correlation between $L_{H\alpha}$ and L_{acc} derived for stars and fixing $M_p = 5 M_J$ and $R_p = 1.5 R_J$, [Zurlo et al. \(2020\)](#) converted the $L_{H\alpha}$ non-detections to accretion rate upper limits $\dot{M} \lesssim 10^{-10}$ – $10^{-9} M_J \text{ yr}^{-1}$ for most systems. For those luminosity upper limits, our model for $M_p = 5 M_J$ implies instead $\dot{M} \lesssim 10^{-8}$ – $10^{-7} M_J \text{ yr}^{-1}$ (see Figure 9). This is thus less constraining by a factor of ~ 100 , which is due to the lower conversion efficiency from accretion energy to $H\alpha$ in the planetary case compared to YSOs as commented by [Zurlo et al. \(2020\)](#), see below and [Aoyama et al. submitted](#)).

How do these limits of $\dot{M} \lesssim 10^{-8}$ – $10^{-7} M_J \text{ yr}^{-1}$ compare to the classical predictions from formation calculations, which can reach up to $\dot{M} \sim 10^{-4.5} M_J \text{ yr}^{-1}$ and had motivated our range of considered \dot{M} values (Section 3.2)?

0. From direct-imaging surveys, several- M_J objects at tens of au or more are known to be intrinsically rare (e.g., [Bowler 2016](#); [Nielsen et al. 2019](#); [Vigan et al. 2020](#)), and the $H\alpha$ surveys cited above have looked at a relatively small number (less than two dozen) targets. They were mostly selected based on a higher assumed likelihood of harbouring a companion, but with uncertain evidence. Therefore, as mentioned by [Zurlo et al. \(2020\)](#), one obvious possibility is that there are in fact no companions outside of the inner working angle of detectors up to now (≥ 100 mas; [Close 2020](#)). This would leave the \dot{M} of forming planets unconstrained by the $H\alpha$ survey results. The absence of distant gas giants is predicted by classical core accretion theories (e.g., [Ikoma et al. 2000](#); [Thommes et al. 2008](#)).

One can *assume* on the contrary that there are companions around the observed stars, and explore what the (\dot{M} , M_p) upper limits imply. Forming a $5\text{-}M_J$ object at a constant $\dot{M} \sim 10^{-7} M_J \text{ yr}^{-1}$ (i.e., a typical super-Jupiter mass at roughly the maximum rate consistent with the non-detections) would require 50 Myr. Given the canonical characteristic disc lifetime of 3 Myr ([Haisch et al. 2001](#); see brief review in [Silverberg et al. 2020](#)), this seems unrealistically long. Conversely, for a constant $\dot{M} \sim 10^{-6} M_J \text{ yr}^{-1}$, which would allow a $5\text{-}M_J$ planet to form within 5 Myr, the model luminosities reach up to $L_{H\alpha} \sim 10^{-5} L_\odot$ (Figure 9), which is roughly 1–2 dex higher than the observational upper limits. Clearly, either there are no planets as mentioned above, or another explanation is needed. Possibilities include:

1. Planets do undergo a phase of classical runaway accretion at high \dot{M} , which is short and unlikely to be observed. For a duration of this “Phase III” of $t_{III} \sim 10^4$ yr to at the very most 10^5 yr (e.g., [Pollack et al. 1996](#); [Mordasini et al. 2014](#)), on the order of $\sim \text{Myr}/t_{III} \sim$ several tens to hundreds of stars would need to be observed to expect catching a planet undergoing runaway accre-

tion. This is reflected in the luminosity statistics in [Mordasini et al. \(2017\)](#), which show only a very small fraction of planets at high luminosity at a given time. On the other hand, given that most targets were selected because of the presence of a gap in the PPDs, the companions could have already grown to a sufficiently large mass to open a gap in an early and short phase of high \dot{M} , provided the gaps are due to planets. They would currently be accreting at an arbitrarily low rate in a late-stage accretion phase (e.g., [Tanigawa & Ikoma 2007](#); [Tanigawa & Tanaka 2016](#)) below the observational limits.

2. Gas-giant masses $M_p \gtrsim M_J$ are reached even earlier on, in the “infall phase” of star formation, in which the whole protoplanetary disc is still heavily enshrouded and thus opaque to emission lines. This is a more dramatic form of the previous possibility. There are some indications that not only the solid building blocks of planets but also M_J -mass planets may be assembled already by ≈ 1 Myr or earlier ([Greaves & Rice 2010](#); [Nixon et al. 2018](#); [Manara et al. 2018](#); [Concha-Ramírez et al. 2021](#); [Küffmeier et al. 2017](#); [Alves et al. 2020](#); for the gravitational instability (GI) mode of planet formation, [Schib et al. 2021](#) found that fragmentation possibly begins early). This lends some qualitative support to the “embedded” hypothesis. However, whether this scenario is plausible quantitatively would need to be studied separately.
3. As a variation and generalisation of the above, planets accrete with *several* phases of “arbitrarily” high \dot{M} , but with again a short total time at high \dot{M} , making detection unlikely. This could occur in the context of episodic accretion (e.g., [Lubow & Martin 2012](#); [Brittain et al. 2020](#); [Martin et al. 2021](#)), with a short duty cycle to allow planets to evade detection. For YSOs, episodic accretion is thought to provide on average roughly 10% of the stellar mass (see brief review in [Kadam et al. 2021](#) and references therein), but the situation could possibly be different for planets.
4. The accretion rate \dot{M} is high but only a small fraction of at most 10^{-2} – 10^{-1} (the inverse of the 1–2 dex difference quoted above) undergoes an accretion shock with sufficiently high preshock velocity $v_0 \gtrsim 30 \text{ km s}^{-1}$ (Section 2.2). This could occur if, as in Section 5.2, most gas hits the (thick) CPD relatively far from the planet, perhaps due to angular momentum effects, and there is no surface shock. This was studied in [Aoyama et al. \(2018\)](#). A limiting case is that planets accrete only by boundary-layer accretion, so that no shock exists and no hydrogen emission lines are produced.

5. Contrary to what is always assumed, it does not hold that $L = 4\pi d^2 F$ for a distance d to the source and flux at the detector F . This issue, which is more difficult to treat, could come from radiative-transfer effects related to the viewing geometry. In particular, the $H\alpha$ emission could be anisotropic (e.g., because $f_{\text{fill}} \neq 1$) or there could be no significant absorption within the system (accretion flow or upper layers of the PPD) that would make the radiation isotropic. However, this is a double-edged possibility, because we could also be observing from a direction into which the emitted flux per unit solid angle is less than $L/4\pi$, exacerbating the discrepancy. Detailed radiative transfer modeling of at least a handful of systems could shed some light on this issue.
6. Planets in fact do accrete at a high \dot{M} but our model predicts too high an efficiency in converting accretion energy into $H\alpha$ emission. While this cannot be excluded in general, we do not see obvious approximations or simplifications in our model that could lead to fluxes several orders of magnitude too high. We point out that our model is already less efficient, by roughly 0.5–2 dex, than the [Rigliaco et al. \(2012\)](#) or [Alcalá et al. \(2017\)](#) empirical stellar correlations ([Aoyama et al. submitted](#)). Thus also here there is no heuristic indication that our $L_{H\alpha}/L_{\text{acc}}$ would be too high.

All of these scenarios are not mutually exclusive. The observational limits on \dot{M} however do not seem to allow for a prolonged phase of moderate accretion ($\dot{M} \sim 10^{-7} - 10^{-5} M_{\text{J}} \text{ yr}^{-1}$) suggested by [Ginzburg & Chiang \(2019\)](#) and that would be responsible for most of the mass of the planet. Alternatively, this phase could be taking place but closer in to the star, going back to the first possibility mentioned above.

In summary, the low observed upper limits on the $H\alpha$ luminosity of possible planets can be explained simply by their absence. This would be unsurprising given the statistical results of direct-imaging surveys that large-separation gas giants are rare and the theoretically predicted slow growth of gas giants in outer protoplanetary discs. If instead the planets *are* present, they could have a time-dependent accretion rate, whether it be high at the beginning of formation first and low later or instead alternatingly high and low during the main phase. Another possibility would be for the $H\alpha$ emission from high- \dot{M} planets to get redirected away from the observer. Statistics based on a higher number of (non-)detections (see [Close 2020](#) for optimistic predictions), as well as tighter constraints closer in to the host stars, should help clarify the relative importance of each aspect.

7. SUMMARY AND CONCLUSIONS

Motivated by recent detections of accretion signatures at young planets or very-low-mass objects ([Keppler et al. 2018](#);

[Wagner et al. 2018](#); [Haffert et al. 2019](#); [Eriksson et al. 2020](#)), we have extended the NLTE shock emission model of [Aoyama et al. \(2018\)](#) to the case that only the planet surface, as opposed to the circumplanetary disc, is the origin of the hydrogen lines. By combining the shock spectrum with models for the photospheric emission, we predict global SEDs (UV to IR) of accreting planets. A possible contribution from the CPD, relevant at far IR wavelengths (e.g., [Zhu 2015](#)), is not included. Extinction by the accreting material or the CPD or PPD is neglected in this work, which we argued (Section 2.3) is a relevant case on its own and allows us to deal with the complex issue of extinction separately in [Marleau et al. \(subm.\)](#).

The formation-relevant input parameters of our model are the accretion rate \dot{M} , the planet mass M_{p} , the planet radius R_{p} , and the filling factor of the accreting region f_{fill} . To provide guidance, we have fit the radius of forming planets as a simple but non-monotonic function of (\dot{M}, M_{p}) from the results of detailed planet structure calculations (Section 2.1.1). While the structure calculations are not definitive, the fit is an improvement over using a constant radius as is often done. Other $R_{\text{p}}(\dot{M}, M_{\text{p}})$ relations could be used.

The photospheric effective temperature T_{eff} was derived approximately self-consistently¹⁴ from the energy transport from the shock model (Section 2.1.2). Because the shock heats the planet, T_{eff} can easily reach 3000–5000 K for the chosen ranges of \dot{M} and M_{p} values.

Fixing $f_{\text{fill}} = 1$, we have scanned the large parameter space and shown global SEDs of forming planets (Figure 8). We have also displayed line luminosities as a function of \dot{M} and M_{p} for individual hydrogen lines, focusing on $H\alpha$ as well as $H\beta$, $\text{Pa}\alpha$, $\text{Pa}\beta$, $\text{Pa}\gamma$, $\text{Br}\alpha$, and $\text{Br}\gamma$ (Figures 9 and 12) and discussing their ratios (Figure 13). The data for these and other hydrogen lines are available upon request.

Our main findings are the following:

1. Despite the high T_{eff} of the planet heated by the shock, the shock contribution to the narrow and broad $H\alpha$ filters of SPHERE and MagAO dominates over the photospheric contribution (Figure 7).
2. At the surface of the planet, the Lyman and Balmer series clearly emerge above the photosphere over all parameter space, and the Paschen continuum is visible at low accretion rates. Details depend on the T_{eff} fit but many lines in the Paschen, Brackett, or other series are visible above the hot photosphere (Figure 8).
3. The $H\alpha$ line luminosity as a function of \dot{M} and M_{p} is a monotonic function of both and makes it possible

¹⁴In the “Suite of Tools to Model Observations of accRetIng planeTZ” (St-Moritz) at <https://github.com/gabrielastro/St-Moritz>, the R_{p} and T_{eff} functions are implemented.

to constrain mostly \dot{M} given an observed value (Figure 9). This is one of the key results. Applying this tool to current detections yields reasonable constraints (Section 4). For example, the mass accretion rate of PDS 70 b is estimated as $\dot{M} = (1.1 \pm 0.3) \times 10^{-8} M_J \text{ yr}^{-1}$ from $L_{H\alpha} = (3.3 \pm 0.1) \times 10^{-7} L_\odot$ (Haffert et al. 2019). The degeneracy between \dot{M} and M_p can be lifted at sufficiently high resolution, higher than afforded by MUSE (Aoyama & Ikoma 2019; Thanathibodee et al. 2019).

4. If there is an accretion shock both on the planet surface and on a circumplanetary disk, the signal is likely to be dominated by the surface-shock contribution. The two shocks are expected to be spectrally distinguishable, with the CPD shock narrower. For PDS 70 b, the resolution of MUSE is not sufficient, but the minimum requirement depends on how sensitive future instruments are to the wings of the $H\alpha$ line (Figure 11).
5. The line luminosity of other transitions such as $H\beta$, $\text{Pa}\alpha$, $\text{Pa}\beta$, $\text{Pa}\gamma$, $\text{Br}\alpha$, or $\text{Br}\gamma$ is a monotonic function of \dot{M} and M_p (Figure 12). We compare this to upper limits for PDS 70 b and the TW Hydra disk. The intensity ratios of these lines to $H\alpha$ range between 10^{-3} and ≈ 1 (Figure 13), and their measurement can yield some constraints on the amount of extinction (Hashimoto et al. 2020).
6. Recent $H\alpha$ surveys have resulted in non-detections of planets outside of ≈ 15 au (≥ 100 mas). Applying the extrapolated YSO $L_{\text{acc}}-L_{H\alpha}$ relationship of Rigliaco et al. (2012) yields upper limits on the instantaneous accretion rate of $\dot{M} \lesssim 10^{-10}-10^{-9} M_J \text{ yr}^{-1}$ (Zurlo et al. 2020), but using our models made explicitly for planets implies instead $\dot{M} \lesssim 10^{-8}-10^{-7} M_J \text{ yr}^{-1}$, which is a less strict constraint, assuming that planets indeed are present are the surveyed stars (Section 6.5).

We point out that a determination of \dot{M} from accretion tracers yields a lower limit on the total accretion rate; the rest of the accreting mass could be joining the planet without a shock at all (e.g., by boundary-layer accretion) or with a shock with too-low velocity $v_0 \gtrsim 30 \text{ km s}^{-1}$ (Sections 2.2.1 and 5.2).

In companion papers, we discuss the use of spectrally-resolved line profiles for inferring the physical parameters of planets (Aoyama & Ikoma 2019), study the correlation between $L_{H\alpha}$ and the accretion luminosity L_{acc} in the planetary case (Aoyama et al. submitted), and assess the absorption of the $H\alpha$ flux by the infalling gas and dust (Marleau et al. *subm.*). These models are applied to PDS 70 b also in Hashimoto et al. (2020) and to Delorme 1 (AB) b in Eriksson et al. (2020).

In Aoyama et al. (submitted), we compare our work to other recent models for the $H\alpha$ emission associated with accreting planets (Thanathibodee et al. 2019; Szulágyi & Ercolano 2020). We emphasise that the postshock electron populations cannot reach equilibrium as the gas cools (Aoyama et al. 2018). This and other radiative properties invalidate the key assumptions behind Storey & Hummer (1995), which was developed for a physically very different context (e.g., planetary nebulae or H II regions). Thus Storey & Hummer (1995) is not appropriate for hydrogen-line luminosity predictions for the planetary accretion shock (Appendix A). For the stellar context too, Storey & Hummer (1995) has been suggested to not be appropriate (e.g., Edwards et al. 2013; Rigliaco et al. 2015; Antonucci et al. 2017), despite its use in earlier analyses.

Continued searches with existing and upcoming or proposed instruments are expected not only to reveal more sources, but will hopefully also increase the number of detected lines. The first group includes the ZIMPOL subsystem of VLT/SPHERE (Beuzit et al. 2008; Schmid et al. 2018), as well as VLT/MUSE (Bacon et al. 2010), LBT/MagAO (Close et al. 2014a,b), SCEXAO/VAMPIRES (Uyama et al. 2020), while to the planned instruments belong MagAO-X (Males et al. 2018; Close et al. 2018; Close 2020), KPIC (Jovanovic et al. 2019; Morris et al. 2020), VIS-X (for $H\alpha$ with $R = 15,000$; PI: S. Haffert, *priv. comm.*), RISTRETTO¹⁵ on the VLT and later possibly on the ELT (with $R > 130,000$, possibly up to $R = 150,000$, covering $H\alpha$; PI: Ch. Lovis; Chazelas et al. 2020), NIRSpec¹⁶ on the *James Webb Space Telescope* (JWST; but note the moderate resolution $R \approx 1000-2700$ and likely high demand for time), HARMONI¹⁷ on the ELT (a first-light IFU that will cover $H\alpha$ at $R = 3000$ and $\lambda = 0.8-2 \mu\text{m}$ at $R = 7000$ or $R = 17,000$), and HIRES/ELT (a second-generation spectrometer planned to cover $1-1.8 \mu\text{m}$ at $R = 100,000$; Marconi et al. 2018; Tozzi et al. 2018, E. Oliva 2020, *priv. comm.*). Combined with simulations of forming planets, these rich data sets are poised to help constrain observationally the complex accretion geometry and ultimately the origin of gas giants.

¹⁵ See <https://zenodo.org/record/3356296>.

¹⁶ See <https://jwst-docs.stsci.edu/near-infrared-spectrograph>.

¹⁷ See <https://harmoni-elt.physics.ox.ac.uk>.

ACKNOWLEDGMENTS

We wish to pay tribute to France Allard, who passed away unexpectedly in October 2020. Her world-leading atmospheric models are used widely in the observational and theoretical communities, and are an important input in this work too. Her kind nature and expertise will be missed by many. We thank R. van Boekel, M. Keppler, A. Müller, J. Bouwman, B. Husemann, M. Samland, D. Homeier, H. M. Schmid, J. Milli, J. Girard, S. Quanz, G. Cugno, T. Stolker, S. Edwards, L. Venuti, B. Stelzberg, Ch. Rab, C. Manara, N. Turner, W. Béthune, M. Bonnefoy, S. Kraus, and O. Ernesto for useful discussions and explanations, insightful questions, and helpful sharing of data. YA was supported by the Leading Graduate Course for Frontiers of Mathematical Sciences and Physics. G-DM acknowledges the support of the German Science Foundation (DFG) priority program SPP 1992 “Exploring the Diversity of Extrasolar Planets” (KU 2849/7-1). G-DM and CM acknowledge support from the Swiss National Science Foundation under grant BSSGI0_155816 “PlanetsInTime”. Parts of this work have been carried out within the framework of JSPS Core-to-Core Program “International Network of Planetary Science (Planet²)” and the NCCR PlanetS supported by the Swiss National Science Foundation. This research has made use of the SVO Filter Profile Service (<http://svo2.cab.inta-csic.es/theory/fps/>) supported by the Spanish MINECO through grant AYA2017-84089 (Rodrigo et al. 2012; Rodrigo & Solano 2020). This research was supported in part by the Japanese–German visitor program of the NCCR PlanetS and by the visitor program of the German Science Foundation (DFG) priority program SPP 1992.

APPENDIX

A. RELATION BETWEEN OUR MODELS AND CASE B (BAKER & MENZEL 1938; STOREY & HUMMER 1995)

The work of Hummer & Storey (1987) and Storey & Hummer (1995, hereafter SH95), based on the Case B model for radiative recombination and ionization (Baker & Menzel 1938), was developed for regions illuminated by a photoionising source such as planetary nebulae and H II regions. Case B assumes that the gas is optically thick to photons from the Lyman series but that all other transitions are optically thin. Also, SH95 assume that the distribution of electron level populations is in an equilibrium. At high densities, this distribution is set by radiative de-excitation balancing collisional excitation¹⁸.

The emissivity tables of SH95 have been used to analyze accretion line intensities or their ratios in the context of

CTTS (e.g., Kóspál et al. 2011) but recent detailed comparisons to observations indicate that this is in fact problematic. The inferred temperatures and densities of the hydrogen-line emitting regions are surprisingly diverse across sources, the line ratios can be far from the model predictions, and many lines are in fact optically thick, making SH95 non-applicable (Kóspál et al. 2011; see the review and detailed comparisons in Edwards et al. 2013; Antonucci et al. 2017; see Section 4.3 of Rigliaco et al. 2015). Recently, Szulágyi & Ercolano (2020) used SH95 to calculate hydrogen line emissivities from accreting planets.

The main reason why the approach of SH95 cannot be used for the planetary- or CPD-surface shock is an issue of timescales. In the cooling region below the hydrodynamic shock, i.e., in the NLTE layers, the cooling timescale t_{cool} is comparable to—and not much longer than—the timescale over which the electron level populations change, t_{pop} . In the usual case that t_{pop} is set by collisions, this is a trivial statement: collisions set the populations and at the same time are the mechanism by which the gas cools. Namely,

¹⁸ At low densities, it is radiative recombination (electrons recombining directly or indirectly into the $n = 3$ level) that populate the $n = 3$ level, but again balanced by radiative de-excitation.

$t_{\text{cool}} \approx E_{\text{int}}/\Lambda$, where E_{int} is the internal energy of the gas and Λ is the cooling rate. In turn, Λ is given by the energy difference between the levels¹⁹ ΔE divided by the timescale for the transition t_{pop} . Thus $t_{\text{cool}} \approx E_{\text{int}}/\Lambda \approx E_{\text{int}}/(\Delta E/t_{\text{pop}})$, such that $t_{\text{cool}}/t_{\text{pop}} \approx E_{\text{int}}/\Delta E$, which is around unity for $\Delta E \approx 10$ eV and the disequilibrium temperatures $T \approx 10^5$ K found in the cooling region (Figure 6). Thus, the gas cools faster than an equilibrium distribution of electrons could be reached; equilibrium would require $t_{\text{pop}} \ll t_{\text{cool}}$ to let the populations adapt to the changing ambient conditions. The fact that $t_{\text{pop}} \sim t_{\text{cool}}$ makes SH95 inapplicable to our case.

For T Tauri stars the situation is likely different, if the gas along the entire accretion funnel is the source of the hydrogen-line emission as Muzerolle et al. (2001) assume. (The H α line in particular could also have a component originating near the shock.) In that case, the temperature and density of a parcel of gas in the accretion-flow region change on the free-fall (dynamical) timescale, which is sufficiently long for equilibrium to be established.

There is a further, secondary, issue with SH95 for the planetary case, concerning the optical depth of the emission lines in the postshock region from where they originate. As mentioned in Section 5.1 and shown in Figure 10, in several cases the H α line is not optically thin in the postshock region, especially towards high preshock number densities n_0 . This is clear given the fact that H α is often optically thick in the accretion flow onto CTTS and that in the planetary case at least the immediate preshock density is higher: from Equation (9), the ratio of typical number densities is

$$\frac{n_{0, \text{planet}}}{n_{0, \text{star}}} \sim \frac{10^{-5} M_{\text{J}} \text{ yr}^{-1}}{10^{-8} M_{\odot} \text{ yr}^{-1}} \sqrt{\frac{0.5 M_{\odot}}{5 M_{\text{J}}} \left(\frac{2 R_{\odot}}{2 R_{\text{J}}}\right)^3} \sim 300, \quad (\text{A1})$$

for the same filling factor. (For reference, a typical ratio of preshock velocities is

$$\frac{v_{0, \text{planet}}}{v_{0, \text{star}}} \sim \sqrt{\frac{5 M_{\text{J}}}{0.5 M_{\odot}} \frac{2 R_{\odot}}{2 R_{\text{J}}}} \sim 0.1 \quad (\text{A2})$$

from Equation (7).) Thus a fundamental assumption of SH95 is fulfilled in some case but in several it is not.

A minor third difference is that in the cooling region below the hydrodynamic shock (i.e., in the Zel’dovich spike), the timescale for *collisional* de-excitation can become smaller (and thus sets the population) than for *radiative* de-excitation. The electron population then tends to the Boltzmann equilibrium distribution and not to the equilibrium assumed in SH95. They were concerned mainly with lower densities, in which case the collisional de-excitations do not play a role, whereas

they can in our case. These effects change the excitation degree and hence the intensity of the emitted H α .

In summary, there are several reasons why the tables of SH95 do not apply to the shock emission of accreting planets. This highlights the need for a “zero-dimensional” time-dependent NLTE Lagrangian radiation-hydrodynamics model (equivalent to a steady-state 1D Eulerian approach) as we have developed and applied to the CPD-surface shock (Aoyama et al. 2018) and the planet-surface shock (this work).

B. INVERSE RELATION BETWEEN THE SHOCK-MICROPHYSICAL AND PLANET-FORMATION (MACROPHYSICAL) PARAMETERS

For completeness, we show in Figure 14 lines of constant \dot{M} and M_{p} in the (n_0, v_0) or (n_0, ρ_0) plane. In the warm case, because of the larger radii, the upper right corner (high preshock density and velocity) is not reached, contrary to the cold case. Except for this, however, in both cases the same part of parameter space is covered.

C. H ALPHA LUMINOSITY AS A FUNCTION OF ACCRETION RATE AND MASS: COLD-START FIT

In Figure 15 we show contours as in Figure 9 but for the cold-start radii (colour and solid contours). They are very similar to the contours for the hot-start case.

D. H α LUMINOSITY DERIVED FROM THE DATA OF WAGNER ET AL. (2018)

Wagner et al. (2018) do not report the H α luminosity of PDS 70 b explicitly but they write that they followed the approach of Close et al. (2014a). Thus their luminosity, assuming isotropic emission, is given by

$$L_{\text{H}\alpha} = 4\pi D^2 \times 10^{A_{\text{R}}} \times C_{\text{H}\alpha} 10^{-R_{\text{A}}/2.5} V_0 W_{\text{f}}, \quad (\text{D3})$$

where $C_{\text{H}\alpha} = (1.14 \pm 0.47) \times 10^{-3}$ is the contrast of the H α signal at the planet’s position to the signal from the primary star in the adjacent continuum (the R band; Wagner et al. 2018), A_{R} is the extinction in the R band, $D = 113.43 \pm 0.52$ pc is the distance of the system (Gaia Collaboration et al. 2018), $V_0 = 2.339 \times 10^{-5} \text{ erg s}^{-1} \text{ cm}^{-2} \mu\text{m}^{-1}$ is the zero-point of the Vega magnitude system in the MagAO H α filter and $W_{\text{f}} = 0.006 \mu\text{m}$ is the filter width (Close et al. 2014a), and $R_{\text{A}} = 11.7 \pm 0.4$ mag is the R band magnitude of PDS 70 A (Henden et al. 2015; Wagner et al. 2018), respectively. Taking the case of no extinction ($A_{\text{R}} = 0$ mag; see below), we obtain for the companion

$$L_{\text{H}\alpha} = (1.4 \pm 0.6) \times 10^{-6} L_{\odot}. \quad (\text{D4})$$

The relative error on this $L_{\text{H}\alpha}$ is dominated by the relative uncertainty on the contrast ($C_{\text{H}\alpha}$). For the contrast itself we

¹⁹In our case, the Ly α transition is responsible for most of the cooling, such that $\Lambda \approx \Lambda_{\text{Ly}\alpha}$, where $\Lambda_{\text{Ly}\alpha}$ is given by Equation (B5) of Iida et al. 2001. Then, $\Delta E = 10.2$ eV. See Figure 6d for an example of Λ .

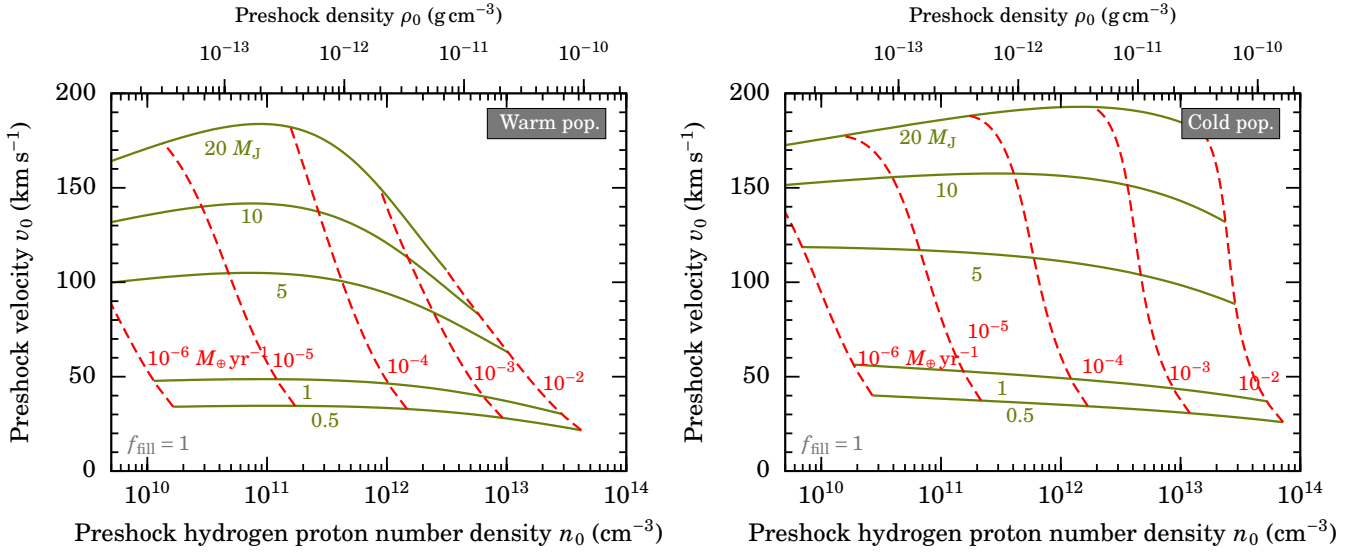


Figure 14. Shock parameter space (n_0, v_0) or (ρ_0, v_0) covered by our grid (Equation (25)), using Equations (7)–(9) and the radius fit of Equation 1 for the warm (*left panel*) and the cold (*right panel*) population respectively. Lines of constant \dot{M} (dashed) and M_p (solid) are labeled. We fix $f_{\text{fill}} = 1$.

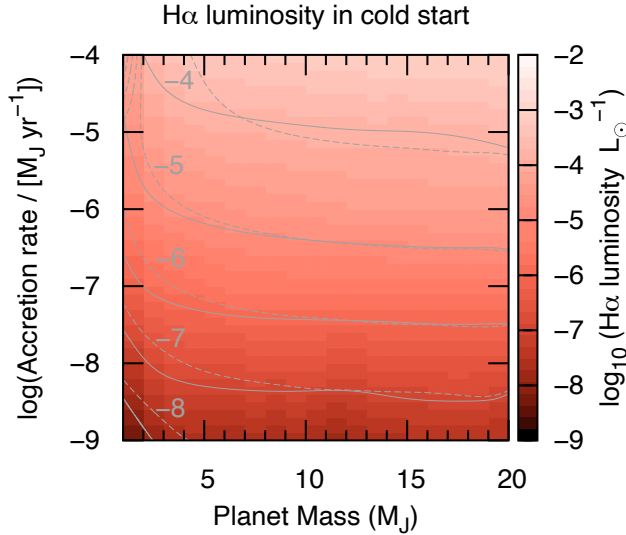


Figure 15. Same as Figure 9 but for the cold-start radius fit. The dashed gray contours show the hot-start results of Figure 9.

used value from the “combined image”. This value agrees with the value of [Thanathibodee et al. \(2019\)](#), $L_{\text{H}\alpha} = (1.3 \pm 0.7) \times 10^{-6} L_{\odot}$ assuming the same distance.

Equation (D4) is confirmed by Equation (7) of [Close \(2020\)](#), which appeared while this work was in preparation. However, [Close \(2020\)](#) mentions an upper limit on A_R of 0.2 mag and uses this as the value of A_R , leading to $L_{\text{H}\alpha} = 2.0 \times 10^{-6} L_{\odot}$. This value of A_R seems too high given the determination of [Müller et al. \(2018\)](#) based on fits to the stellar spectrum using the detailed MIST models ([Dotter 2016](#); [Choi et al. 2016](#)), which yielded $A_V = 0.05^{+0.05}_{-0.03}$ mag and thus $A_R = 0.06^{+0.06}_{-0.04}$ mag using the [Cardelli et al. \(1989\)](#) law with $R = 3.1$ for typical ISM dust. This agrees with the results of the *Stilism* statistical tool under <https://stilism.obspm.fr> ([Lallement et al. 2019](#)), $E(B - V) = 0.01^{+0.02}_{-0.01}$ mag in the direction and at the distance of PDS 70 A, which similarly implies $A_R = 0.04^{+0.07}_{-0.04}$ mag.

REFERENCES

- Alcalá, J. M., Natta, A., Manara, C. F., et al. 2014, *A&A*, 561, A2
 Alcalá, J. M., Manara, C. F., Natta, A., et al. 2017, *A&A*, 600, A20
 Alibert, Y., Mordasini, C., Benz, W., & Winisdoerffer, C. 2005, *A&A*, 434, 343
 Allard, F., Homeier, D., & Freytag, B. 2012, *Philosophical Transactions of the Royal Society of London Series A*, 370, 2765
 Alves, F. O., Cleeves, L. I., Girart, J. M., et al. 2020, *ApJL*, 904, L6
 Antonucci, S., Nisini, B., Giannini, T., et al. 2017, *A&A*, 599, A105
 Aoyama, Y., & Ikoma, M. 2019, *ApJL*, 885, L29
 Aoyama, Y., Ikoma, M., & Tanigawa, T. 2018, *ApJ*, 866, 84
 Aoyama, Y., Marleau, G.-D., Ikoma, M., & Mordasini, C. submitted, *ApJL*

- Bacon, R., Accardo, M., Adjali, L., et al. 2010, in *Society of Photo-Optical Instrumentation Engineers (SPIE) Conference Series*, Vol. 7735, *Ground-based and Airborne Instrumentation for Astronomy III (SPIE)*, 773508
- Bae, J., Zhu, Z., Baruteau, C., et al. 2019, *ApJL*, 884, L41
- Baker, J. G., & Menzel, D. H. 1938, *ApJ*, 88, 52
- Baraffe, I., Homeier, D., Allard, F., & Chabrier, G. 2015, *A&A*, 577, A42
- Baruteau, C., Bai, X., Mordasini, C., & Mollière, P. 2016, *SSRv*, 205, 77
- Batygin, K. 2018, *AJ*, 155, 178
- Berardo, D., & Cumming, A. 2017, *ApJL*, 846, L17
- Berardo, D., Cumming, A., & Marleau, G.-D. 2017, *ApJ*, 834, 149
- Béthune, W. 2019, *MNRAS*, 490, 3144
- Beuzit, J.-L., Feldt, M., Dohlen, K., et al. 2008, in *Proc. SPIE*, Vol. 7014, *Ground-based and Airborne Instrumentation for Astronomy II*, 701418
- Bodenheimer, P., Hubickyj, O., & Lissauer, J. J. 2000, *Icarus*, 143, 2
- Bonnefoy, M., Chauvin, G., Lagrange, A. M., et al. 2014, *A&A*, 562, A127
- Bowler, B. P. 2016, *PASP*, 128, 38
- Bowler, B. P., Liu, M. C., Kraus, A. L., & Mann, A. W. 2014, *ApJ*, 784, 65
- Brittain, S. D., Najita, J. R., Dong, R., & Zhu, Z. 2020, *ApJ*, 895, 48
- Calvet, N., & Gullbring, E. 1998, *ApJ*, 509, 802
- Cardelli, J. A., Clayton, G. C., & Mathis, J. S. 1989, *ApJ*, 345, 245
- Chazelas, B., Lovis, C., Blind, N., et al. 2020, in *Society of Photo-Optical Instrumentation Engineers (SPIE) Conference Series*, Vol. 11448, *Society of Photo-Optical Instrumentation Engineers (SPIE) Conference Series*, 1144875
- Chinchilla, P., Béjar, V. J. S., Lodieu, N., Zapatero Osorio, M. R., & Gauza, B. 2021, *A&A*, 645, A17
- Choi, J., Dotter, A., Conroy, C., et al. 2016, *ApJ*, 823, 102
- Christensen, U. R., Holzwarth, V., & Reiners, A. 2009, *Nature*, 457, 167
- Christiaens, V., Cantalloube, F., Casassus, S., et al. 2019a, *ApJL*, 877, L33
- Christiaens, V., Casassus, S., Absil, O., et al. 2019b, *MNRAS*, 486, 5819
- Ciddor, P. E. 1996, *Appl. Opt.*, 35, 1566
- Cleeves, L. I., Bergin, E. A., & Harries, T. J. 2015, *ApJ*, 807, 2
- Close, L. M. 2020, *AJ*, 160, 221
- Close, L. M., Follette, K. B., Males, J. R., et al. 2014a, *ApJL*, 781, L30
- Close, L. M., Males, J. R., Follette, K. B., et al. 2014b, in *Society of Photo-Optical Instrumentation Engineers (SPIE) Conference Series*, Vol. 9148, *Adaptive Optics Systems IV*, 91481M
- Close, L. M., Males, J. R., Durney, O., et al. 2018, in *Society of Photo-Optical Instrumentation Engineers (SPIE) Conference Series*, Vol. 10703, *Adaptive Optics Systems VI*, 107034Y
- Concha-Ramírez, F., Wilhelm, M. J. C., Zwart, S. P., van Terwisga, S. E., & Hacar, A. 2021, *MNRAS*, 501, 1782
- Cox, A. N. 2000, *Allen's astrophysical quantities* (New York: AIP Press, Springer)
- Cugno, G., Quanz, S. P., Hunziker, S., et al. 2019, *A&A*, 622, A156
- Cumming, A., Helled, R., & Venturini, J. 2018, *MNRAS*, 477, 4817
- Currie, T., Cloutier, R., Brittain, S., et al. 2015, *ApJL*, 814, L27
- Currie, T., Marois, C., Cieza, L., et al. 2019, *ApJL*, 877, L3
- Delorme, P., Gagné, J., Girard, J. H., et al. 2013, *A&A*, 553, L5
- Dong, J., Jiang, Y.-F., & Armitage, P. 2020, arXiv e-prints, arXiv:2012.06641
- Dotter, A. 2016, *ApJS*, 222, 8
- Drake, R. P. 2006, *High-Energy-Density Physics: Fundamentals, Inertial Fusion, and Experimental Astrophysics* (Springer)
- Edwards, S., Kwan, J., Fischer, W., et al. 2013, *ApJ*, 778, 148
- Eisner, J. A. 2015, *ApJL*, 803, L4
- Emsenhuber, A., Mordasini, C., Burn, R., et al. 2020a, arXiv e-prints, arXiv:2007.05561
- Emsenhuber, A., Mordasini, C., Burn, R., et al. 2020b, arXiv e-prints, arXiv:2007.05562
- Eriksson, S. C., Asensio Torres, R., Janson, M., et al. 2020, *A&A*, 638, L6
- Fang, M., van Boekel, R., Wang, W., et al. 2009, *A&A*, 504, 461
- Gaia Collaboration, Brown, A. G. A., Vallenari, A., et al. 2018, *A&A*, 616, A1
- Ginzburg, S., & Chiang, E. 2019, *MNRAS*, 490, 4334
- Gnat, O., & Ferland, G. J. 2012, *ApJS*, 199, 20
- Greaves, J. S., & Rice, W. K. M. 2010, *MNRAS*, 407, 1981
- Gullbring, E., Hartmann, L., Briceño, C., & Calvet, N. 1998, *ApJ*, 492, 323
- Haffert, S. Y., Bohn, A. J., de Boer, J., et al. 2019, *Nature Astronomy*, 3, 329
- Haisch, Jr., K. E., Lada, E. A., & Lada, C. J. 2001, *ApJL*, 553, L153
- Hansen, C. J., Kawaler, S. D., & Trimble, V. 2004, *Stellar interiors: physical principles, structure, and evolution*, 2nd ed. (New York: Springer-Verlag)
- Hartmann, L., Herczeg, G., & Calvet, N. 2016, *ARA&A*, 54, 135
- Hartmann, L., Hewett, R., & Calvet, N. 1994, *ApJ*, 426, 669
- Hashimoto, J., Aoyama, Y., Konishi, M., et al. 2020, *AJ*, 159, 222
- Helled, R., Bodenheimer, P., Podolak, M., et al. 2014, in *Protostars and Planets VI*, ed. H. Beuther, R. S. Klessen, C. P. Dullemond, & T. Henning, 643
- Henden, A. A., Levine, S., Terrell, D., & Welch, D. L. 2015, in *American Astronomical Society Meeting Abstracts*, Vol. 225, *American Astronomical Society Meeting Abstracts*, 336.16
- Herczeg, G. J., & Hillenbrand, L. A. 2008, *ApJ*, 681, 594

- Herczeg, G. J., Wood, B. E., Linsky, J. L., Valenti, J. A., & Johns-Krull, C. M. 2004, *ApJ*, 607, 369
- Hollenbach, D., & McKee, C. F. 1989, *ApJ*, 342, 306
- Hummer, D. G., & Storey, P. J. 1987, *MNRAS*, 224, 801
- Iida, A., Nakamoto, T., Susa, H., & Nakagawa, Y. 2001, *Icarus*, 153, 430
- Ikoma, M., Nakazawa, K., & Emori, H. 2000, *ApJ*, 537, 1013
- Ingleby, L., Calvet, N., Herczeg, G., et al. 2013, *ApJ*, 767, 112
- Janson, M., Reffert, S., Brandner, W., et al. 2008, *A&A*, 488, 771
- Jovanovic, N., Delorme, J. R., Bond, C. Z., et al. 2019, arXiv e-prints, arXiv:1909.04541
- Kadam, K., Vorobyov, E., & Kóspál, Á. 2021, arXiv e-prints, arXiv:2101.05764
- Kastner, J. H., Huenemoerder, D. P., Schulz, N. S., Canizares, C. R., & Weintraub, D. A. 2002, *ApJ*, 567, 434
- Katarzyński, K., Gawroński, M., & Goździewski, K. 2016, *MNRAS*, 461, 929
- Kenyon, S. J., & Hartmann, L. 1987, *ApJ*, 323, 714
- Keppler, M., Benisty, M., Müller, A., et al. 2018, *A&A*, 617, A44
- Keppler, M., Teague, R., Bae, J., et al. 2019, *A&A*, 625, A118
- Kervella, P., Montargès, M., Ridgway, S. T., et al. 2014, *A&A*, 564, A88
- Kley, W. 1989, *A&A*, 208, 98
- Kley, W. 1999, *MNRAS*, 303, 696
- Komarova, O., & Fischer, W. J. 2020, *RNAAS*, 4, 6
- Königl, A. 1991, *ApJL*, 370, L39
- Kóspál, Á., Ábrahám, P., Goto, M., et al. 2011, *ApJ*, 736, 72
- Kraus, A. L., & Ireland, M. J. 2012, *ApJ*, 745, 5
- Küffmeier, M., Haugbølle, T., & Nordlund, Å. 2017, *ApJ*, 846, 7
- Kwan, J., & Fischer, W. 2011, *MNRAS*, 411, 2383
- Lallement, R., Babusiaux, C., Vergely, J. L., et al. 2019, *A&A*, 625, A135
- Lissauer, J. J., Hubickyj, O., D'Angelo, G., & Bodenheimer, P. 2009, *Icarus*, 199, 338
- Lubow, S. H., & Martin, R. G. 2012, *ApJL*, 749, L37
- Males, J. R., Close, L. M., Miller, K., et al. 2018, in *Society of Photo-Optical Instrumentation Engineers (SPIE) Conference Series*, Vol. 10703, *Adaptive Optics Systems VI*, 1070309
- Manara, C. F., Morbidelli, A., & Guillot, T. 2018, *A&A*, 618, L3
- Manara, C. F., Testi, L., Rigliaco, E., et al. 2013, *A&A*, 551, A107
- Manara, C. F., Testi, L., Herczeg, G. J., et al. 2017, *A&A*, 604, A127
- Marconi, A., Di Marcantonio, P., D'Odorico, V., et al. 2016, in *Society of Photo-Optical Instrumentation Engineers (SPIE) Conference Series*, Vol. 9908, *Proceedings of the SPIE, Volume 9908*, id. 990823 12 pp. (2016). (SPIE), 990823
- Marconi, A., Allende Prieto, C., Amado, P. J., et al. 2018, in *Society of Photo-Optical Instrumentation Engineers (SPIE) Conference Series*, Vol. 10702, *Ground-based and Airborne Instrumentation for Astronomy VII*, ed. C. J. Evans, L. Simard, & H. Takami, 107021Y
- Marleau, G.-D., Klahr, H., Kuiper, R., & Mordasini, C. 2017, *ApJ*, 836, 221
- Marleau, G.-D., Mordasini, C., & Kuiper, R. 2019, *ApJ*, 881, 144
- Marleau, G.-D., Aoyama, Y., Kuiper, R., et al. subm., *A&A*
- Marley, M. S., Fortney, J. J., Hubickyj, O., Bodenheimer, P., & Lissauer, J. J. 2007, *ApJ*, 655, 541
- Martin, R. G., Zhu, Z., Armitage, P. J., Yang, C.-C., & Baehr, H. 2021, *MNRAS*, arXiv:2101.09388 [astro-ph.EP]
- Mendigutía, I., Oudmaijer, R. D., Schneider, P. C., et al. 2018, *A&A*, 618, L9
- Mesa, D., Keppler, M., Cantalloube, F., et al. 2019, *A&A*, 632, A25
- Meshkat, T., Kenworthy, M. A., Quanz, S. P., & Amara, A. 2014, *ApJ*, 780, 17
- Mollière, P., & Mordasini, C. 2012, *A&A*, 547, A105
- Mordasini, C., Alibert, Y., Georgy, C., et al. 2012a, *A&A*, 547, A112
- Mordasini, C., Alibert, Y., Klahr, H., & Henning, T. 2012b, *A&A*, 547, A111
- Mordasini, C., Klahr, H., Alibert, Y., Miller, N., & Henning, T. 2014, *A&A*, 566, A141
- Mordasini, C., Marleau, G.-D., & Mollière, P. 2017, *A&A*, 608, A72
- Mordasini, C., Mollière, P., Dittkrist, K.-M., Jin, S., & Alibert, Y. 2015, *International Journal of Astrobiology*, 14, 201
- Morris, E. C., Wang, J. J., Ruffio, J.-B., et al. 2020, in *Society of Photo-Optical Instrumentation Engineers (SPIE) Conference Series*, Vol. 11447, *Society of Photo-Optical Instrumentation Engineers (SPIE) Conference Series*, 1144761
- Müller, A., Keppler, M., Henning, T., et al. 2018, *A&A*, 617, L2
- Muzerolle, J., Calvet, N., & Hartmann, L. 2001, *ApJ*, 550, 944
- Natta, A., Testi, L., Muzerolle, J., et al. 2004, *A&A*, 424, 603
- Nielsen, E. L., De Rosa, R. J., Macintosh, B., et al. 2019, *AJ*, 158, 13
- Nixon, C. J., King, A. R., & Pringle, J. E. 2018, *MNRAS*, 477, 3273
- Owen, J. E., & Menou, K. 2016, *ApJL*, 819, L14
- Pollack, J. B., Hubickyj, O., Bodenheimer, P., et al. 1996, *Icarus*, 124, 62
- Quanz, S. P., Amara, A., Meyer, M. R., et al. 2013, *ApJL*, 766, L1
- Quanz, S. P., Meyer, M. R., Kenworthy, M. A., et al. 2010, *ApJL*, 722, L49
- Rab, C., Kamp, I., Ginski, C., et al. 2019, *A&A*, 624, A16
- Reggiani, M., Meyer, M. R., Chauvin, G., et al. 2016, *A&A*, 586, A147
- Riaud, P., Mawet, D., Absil, O., et al. 2006, *A&A*, 458, 317

- Rigliaco, E., Natta, A., Testi, L., et al. 2012, *A&A*, 548, A56
- Rigliaco, E., Pascucci, I., Duchene, G., et al. 2015, *ApJ*, 801, 31
- Rodrigo, C., & Solano, E. 2020, in Contributions to the XIV.0 Scientific Meeting (virtual) of the Spanish Astronomical Society, 182
- Rodrigo, C., Solano, E., & Bayo, A. 2012, SVO Filter Profile Service Version 1.0, IVOA Working Draft 15 October 2012
- Rodrigues, M., Capone, J., Earle, A., et al. 2018, in Society of Photo-Optical Instrumentation Engineers (SPIE) Conference Series, Vol. 10702, Ground-based and Airborne Instrumentation for Astronomy VII, ed. C. J. Evans, L. Simard, & H. Takami, 107029M
- Sallum, S., Follette, K. B., Eisner, J. A., et al. 2015, *Nature*, 527, 342
- Sanchis, E., Picogna, G., Ercolano, B., Testi, L., & Rosotti, G. 2020, *MNRAS*, 492, 3440
- Schib, O., Mordasini, C., Wenger, N., Marleau, G. D., & Helled, R. 2021, *A&A*, 645, A43
- Schlaufman, K. C. 2018, *ApJ*, 853, 37
- Schlecker, M., Mordasini, C., Emsenhuber, A., et al. 2020, arXiv e-prints, arXiv:2007.05563
- Schmid, H. M., Bazzon, A., Milli, J., et al. 2017, *A&A*, 602, A53
- Schmid, H. M., Bazzon, A., Roelfsema, R., et al. 2018, *A&A*, 619, A9
- Schmidt, T. O. B., Neuhäuser, R., Seifahrt, A., et al. 2008, *A&A*, 491, 311
- Schulik, M., Johansen, A., Bitsch, B., & Lega, E. 2019, *A&A*, 632, A118
- Schulik, M., Johansen, A., Bitsch, B., Lega, E., & Lambrechts, M. 2020, *A&A*, 642, A187
- Shapiro, P. R., & Kang, H. 1987, *ApJ*, 318, 32
- Silverberg, S. M., Wisniewski, J. P., Kuchner, M. J., et al. 2020, *ApJ*, 890, 106
- Stolker, T., Marleau, G. D., Cugno, G., et al. 2020a, *A&A*, 644, A13
- Stolker, T., Quanz, S. P., Todorov, K. O., et al. 2020b, *A&A*, 635, A182
- Storey, P. J., & Hummer, D. G. 1995, *MNRAS*, 272, 41
- Szulágyi, J., Dullemond, C. P., Pohl, A., & Quanz, S. P. 2019, *MNRAS*, 487, 1248
- Szulágyi, J., & Ercolano, B. 2020, *ApJ*, 902, 126
- Szulágyi, J., & Mordasini, C. 2017, *MNRAS*, 465, L64
- Tanigawa, T., & Ikoma, M. 2007, *ApJ*, 667, 557
- Tanigawa, T., Ohtsuki, K., & Machida, M. N. 2012, *ApJ*, 747, 47
- Tanigawa, T., & Tanaka, H. 2016, *ApJ*, 823, 48
- Thalmann, C., Janson, M., Garufi, A., et al. 2016, *ApJL*, 828, L17
- Thanathibodee, T., Calvet, N., Bae, J., Muzerolle, J., & Hernández, R. F. 2019, *ApJ*, 885, 94
- Thatte, N. A., Clarke, F., Bryson, I., et al. 2016, in Society of Photo-Optical Instrumentation Engineers (SPIE) Conference Series, Vol. 9908, Ground-based and Airborne Instrumentation for Astronomy VI, ed. C. J. Evans, L. Simard, & H. Takami, 99081X
- Thommes, E. W., Matsumura, S., & Rasio, F. A. 2008, *Science*, 321, 814
- Tozzi, A., Oliva, E., Xompero, M., et al. 2018, in Society of Photo-Optical Instrumentation Engineers (SPIE) Conference Series, Vol. 10702, Ground-based and Airborne Instrumentation for Astronomy VII, ed. C. J. Evans, L. Simard, & H. Takami, 107028Q
- Uchida, Y., & Shibata, K. 1984, *PASJ*, 36, 105
- Uyama, T., Tanigawa, T., Hashimoto, J., et al. 2017, *AJ*, 154, 90
- Uyama, T., Norris, B., Jovanovic, N., et al. 2020, *Journal of Astronomical Telescopes, Instruments, and Systems*, 6, 045004
- Valenti, J. A., Basri, G., & Johns, C. M. 1993, *AJ*, 106, 2024
- van Boekel, R., Henning, T., Menu, J., et al. 2017, *ApJ*, 837, 132
- Vaytet, N., González, M., Audit, E., & Chabrier, G. 2013, *JQSRT*, 125, 105
- Venuti, L., Stelzer, B., Alcalá, J. M., et al. 2019, *A&A*, 632, A46
- Vigan, A., Fontanive, C., Meyer, M., et al. 2020, arXiv e-prints, arXiv:2007.06573
- Wagner, K., Apai, D., & Kratter, K. M. 2019, *ApJ*, 877, 46
- Wagner, K., Follette, K. B., Close, L. M., et al. 2018, *ApJL*, 863, L8
- Wang, J. J., Ginzburg, S., Ren, B., et al. 2020, *AJ*, 159, 263
- Wang, J. J., Vigan, A., Lacour, S., et al. 2021, arXiv e-prints, arXiv:2101.04187
- Wu, Y.-L., Close, L. M., Males, J. R., et al. 2015, *ApJ*, 801, 4
- Xie, C., Haffert, S. Y., de Boer, J., et al. 2020, *A&A*, 644, A149
- Yoshii, Y., Aoki, T., Doi, M., et al. 2010, in Society of Photo-Optical Instrumentation Engineers (SPIE) Conference Series, Vol. 7733, Proc. SPIE (Society of Photo-Optical Instrumentation Engineers (SPIE)), 773308
- Zapolsky, H. S., & Salpeter, E. E. 1969, *ApJ*, 158, 809
- Zhou, Y., Herczeg, G. J., Kraus, A. L., Metchev, S., & Cruz, K. L. 2014, *ApJL*, 783, L17
- Zhou, Y., Apai, D., Bowler, B., et al. submitted
- Zhu, Z. 2015, *ApJ*, 799, 16
- Zurlo, A., Cugno, G., Montesinos, M., et al. 2020, *A&A*, 633, A119